



# Reconstructing volcanic radiative forcing since 1990, using a comprehensive emission inventory and spatially resolved sulfur injections from satellite data in a chemistry-climate model

Jennifer Schallock<sup>1</sup>, Christoph Brühl<sup>1</sup>, Christine Bingen<sup>2</sup>, Michael Höpfner<sup>3</sup>, Landon Rieger<sup>4</sup>, and Jos Lelieveld<sup>1</sup>

<sup>1</sup>Atmospheric Chemistry Department, Max Planck Institute for Chemistry, Mainz, Germany

<sup>2</sup>Royal Belgian Institute for Space Aeronomy, Brussels, Belgium

<sup>3</sup>Institute of Meteorology and Climate Research, Karlsruhe Institute of Technology, Karlsruhe, Germany

<sup>4</sup>Institute of Space and Atmospheric Studies, University of Saskatchewan, Saskatoon, Canada

**Correspondence:** Jennifer Schallock (jennifer.schallock@mpic.de)

Received: 4 August 2021 – Discussion started: 16 August 2021

Revised: 16 December 2022 – Accepted: 19 December 2022 – Published: 23 January 2023

**Abstract.** This paper presents model simulations of stratospheric aerosols with a focus on explosive volcanic eruptions. Using various (occultation and limb-based) satellite instruments, providing vertical profiles of sulfur dioxide (SO<sub>2</sub>) and aerosol extinction, we characterized the chemical and radiative influence of volcanic aerosols for the period between 1990 and 2019.

We established an improved and extended volcanic SO<sub>2</sub> emission inventory that includes more than 500 explosive volcanic eruptions reaching the upper troposphere and the stratosphere. Each perturbation identified was derived from the satellite data and incorporated as a three-dimensional SO<sub>2</sub> plume into a chemistry-climate model without the need for additional assumptions about altitude distribution and eruption duration as needed for a “point source” approach.

The simultaneous measurements of SO<sub>2</sub> and aerosol extinction by up to four satellite instruments enabled a reliable conversion of extinction measurements into injected SO<sub>2</sub>. In the chemistry-climate model, the SO<sub>2</sub> from each individual plume was converted into aerosol particles and their optical properties were determined. Furthermore, the aerosol optical depth (AOD) and the instantaneous radiative forcing on climate were calculated online. Combined with model improvements, the results of the simulations are consistent with the observations of the various satellites.

Slight deviations between the observations and model simulations were found for the large volcanic eruption of Pinatubo in 1991 and cases where simultaneous satellite observations were not unique or too sparse. Weak- and medium-strength volcanic eruptions captured in satellite data and the Smithsonian database typically inject about 10 to 50 kt SO<sub>2</sub> directly into the upper troposphere/lower stratosphere (UTLS) region or the sulfur species are transported via convection and advection. Our results confirm that these relatively minor eruptions, which occur quite frequently, can nevertheless contribute to the stratospheric aerosol layer and are relevant for the Earth’s radiation budget. These minor eruptions cause a total global instantaneous radiative forcing of the order of  $-0.1 \text{ W m}^{-2}$  at the top of the atmosphere (TOA) compared to a background stratospheric aerosol forcing of about  $-0.04 \text{ W m}^{-2}$ . Medium-strength eruptions injecting about 400 kt SO<sub>2</sub> into the stratosphere or accumulation of consecutive smaller eruptions can lead to a total instantaneous forcing of about  $-0.3 \text{ W m}^{-2}$ . We show that it is critical to include the contribution of the extratropical lowermost stratospheric aerosol in the forcing calculations.

## 1 Introduction

Next to recent historical events in which large fires have become a major source of aerosols up to the tropopause and above (Kloss et al., 2019), stratospheric aerosol particles are mostly of volcanic origin and consist of an internal liquid mixture of sulfuric acid ( $\text{H}_2\text{SO}_4$ ) and water ( $\text{H}_2\text{O}$ ) (Vernier et al., 2011). The typical median diameter of these aerosol particles ranges between 200 nm for the background aerosol and 600 nm for Pinatubo conditions (Wilson et al., 2008). In this study, we incorporated stratospheric aerosol, the sulfur chemistry and the radiative transfer into a comprehensive chemistry-climate model (CCM), which we have used to gain a better understanding of the interaction of aerosols with the global climate system, including chemical effects. Particular emphasis is being placed on adequately modelling and understanding the impact of volcanic eruptions and other aerosol sources on the evolution of the stratospheric aerosol burden.

Sulfate and ashes from explosive volcanic eruptions can account for the majority of the aerosol burden in the stratosphere during volcanically active periods and cause strong temporal and spatial variations in the concentration and the size distribution of the particles (Vernier et al., 2011). These changes influence in turn the radiative forcing at the top of the atmosphere (or at tropopause altitude) for several years after strong eruptions (Timmreck, 2012) and can even have a more prolonged impact on the global climate (McGregor et al., 2015). After such a volcanic eruption, the enhanced radiative heating in the stratosphere exerts an effect on dynamics, influences the global spread of the volcanic cloud and leads to an upward transport of the aerosol itself as well as other chemical tracers, including ozone (Timmreck et al., 1999). The aerosol radiative heating resulting from large volcanic eruptions like Pinatubo triggers enhanced tropical upwelling, which causes a lofting of the injected  $\text{SO}_2$  (sulfur dioxide) and the aerosol as well as other compounds. The radiative feedback on dynamics is required to model aerosol extinction in the upper part of the volcanic aerosol plume that corresponds to observations (e.g. Aquila et al., 2012; Toohey et al., 2011).

Due to the large variability in volcanic emissions, it is challenging to estimate future trends for stratospheric optical depth and forcing (Swindles et al., 2018; Fasullo et al., 2017; Aubry et al., 2021). Therefore, the influence of volcanic eruptions is not included in predictive simulations for future climate scenarios in the IPCC report of 2013 (IPCC, 2013).

Previous studies show that model simulations often cannot fully reproduce the aerosol optical depth (AOD) of satellite observations or the derived global forcing of the stratospheric aerosol layer (Solomon et al., 2011), because the number of volcanic eruptions reaching the stratosphere and treated explicitly appears to be underestimated in most analyses (Mills

et al., 2016; Brühl et al., 2015; Schmidt et al., 2018; Anderson et al., 2015). Conversely, the intensity of single eruptions can sometimes be overestimated because of incorrect vertical distribution of the injection patterns in the models (e.g. Kasatochi compared to Glantz et al., 2014). In previous studies smaller volcanic eruptions have often been included in the background atmosphere, even though they can be responsible for a radiative forcing that is twice as strong as the non-volcanic background conditions in volcanically quiescent periods such as from 1999 to 2002 (IPCC, 2013; Solomon et al., 2011; Vernier et al., 2011). Friberg et al. (2018) included the entire time series of CALIOP (Cloud-Aerosol Lidar with Orthogonal Polarization) data from 2006 to 2015 and derived stratospheric AOD using reanalysis data for the tropopause but only mention medium-sized eruptions explicitly. Radiative forcing is estimated in this case by multiplying AOD by a factor of  $-25$  (Hansen et al., 2005) rather than using a radiative transfer model, an approximation valid in the absence of major forest fires (see e.g. Sellitto et al., 2022).

The model simulations in this study are compared to GloSAC V2 (Thomason et al., 2018; Kovilakam et al., 2020), a time-dependent multi-satellite zonal average aerosol climatology which provides extinction data (Fig. C1 in Appendix C1). In our approach we consider as much as possible small eruptions reaching the stratosphere explicitly. For this purpose we calculate  $\text{SO}_2$  injections into the stratosphere based on the Smithsonian volcano database and the most recent releases of satellite datasets, in particular those gathered using limb sounding instruments to derive information on the vertical distribution.

For the ENVISAT (European Environmental Satellite) period 2002–2012 a first version of a new volcanic  $\text{SO}_2$  inventory with improved temporal and spatial resolution was developed within the framework of ISAMIP (<https://isamip.eu>, last access: 10 January 2023) (Timmreck et al., 2018; Brühl et al., 2018). The corresponding database ([https://doi.org/10.1594/WDCC/SSIRC\\_1](https://doi.org/10.1594/WDCC/SSIRC_1); Brühl, 2018) contains three-dimensional  $\text{SO}_2$  perturbations derived from satellite data as well as integrated injected  $\text{SO}_2$  masses. In this work the database is expanded to the period 1990–2019 and is considerably improved for the period 1998–2001. The simultaneous measurements from up to four instruments from 2002 to 2012 enabled us to develop a novel procedure for conversion of aerosol extinction to  $\text{SO}_2$  needed for the period before and after ENVISAT.

Our method circumvents problems and uncertainties related to the classical point source approach like dependence on the model grid box size and exact location as well as the assumed vertical distribution, the assumed time interval during which the mass is injected, and effects of microphysical and chemical interactions of  $\text{SO}_2$  and sulfate with injected volcanic ash and water in the early phase (Zhu et al., 2020). Since simulations of point source emissions are very sensi-

tive to the emission conditions, in some cases it may be more appropriate to implement the main plume of volcanic emissions in the model not directly at the volcano location but instead apply other coordinates according to satellite observations. A case study for point source emissions is shown in Appendix C3.

Non-eruptive permanently degassing volcanoes represent another natural source of aerosols, which are treated separately from active explosive volcanic eruptions. For the stratosphere these contribute in most cases only to the background since most but not all of the released  $\text{SO}_2$  is removed by oxidation and rainout in the troposphere and only a small fraction can reach the stratosphere by convection and large-scale transport. This holds also for the medium-sized eruption of Eyjafjallajökull in 2010 from which almost no  $\text{SO}_2$  reached the stratosphere, as shown by MIPAS observations. Stratospheric  $\text{H}_2\text{SO}_4$  is also produced from non-volcanic sulfur precursor gases, like carbonyl sulfide (OCS) (Crutzen, 1976), dimethyl sulfide (DMS) (Kettle and Andreae, 2000), and tropospheric  $\text{SO}_2$  from pollution, which constitute a source of background concentration of stratospheric aerosol.

This paper is structured as follows: Sect. 2 presents satellite data used for entering the volcanic perturbations of aerosols and  $\text{SO}_2$  into the model and for model evaluation. In Sect. 3, the set-up used for the climate model simulations is described. Section 4 contains a volcanic sulfur emission inventory with all relevant explosive volcanic eruptions detected between 1990 and 2019, which are included in the model simulations in Sect. 5. The influence of these volcanic eruptions on the stratosphere and climate is analysed in Sect. 6. At the end of Sect. 6 as well as in the final discussion (Sect. 7), the results are discussed in a wider context.

## 2 Satellite observations

To generate the input data from volcanic eruptions for our simulations, we analysed satellite datasets from two instruments on the European Environmental Satellite (ENVISAT) that was launched on 1 March 2002 and lost signal on 8 April 2012, namely MIPAS ( $\text{SO}_2$  data) and Global Ozone Monitoring by Occultation of Stars (GOMOS – aerosol extinction data). Furthermore, the OSIRIS instrument on board the Odin satellite was used to provide additional aerosol extinction data for the period up to 2019. For the period before 2002, we used the SAGE II instrument for aerosol extinction data. The data processing is described in Sect. 4. Some examples of eruptions where simultaneous observations from all these instruments or at least three were available for cross-validation are presented in Appendix B.

### 2.1 Michelson Interferometer for Passive Atmospheric Sounding (MIPAS)

MIPAS was a mid-infrared emission spectrometer on board the ENVISAT satellite. MIPAS scanned the limb, thereby

analysing the infrared radiation emitted by the Earth's atmosphere at different tangent altitudes (Fischer et al., 2008).

The atmospheric spectra ranging from 4.15 to 14.6  $\mu\text{m}$  are inverted to provide vertical profiles of temperature and volume mixing ratios of more than 25 different trace species, like the sulfate aerosol precursor gases  $\text{SO}_2$  and OCS (Glatthor et al., 2015, 2017; Höpfner et al., 2013, 2015), as well as  $\text{H}_2\text{O}$ , ozone ( $\text{O}_3$ ), methane ( $\text{CH}_4$ ), nitrous oxide ( $\text{N}_2\text{O}$ ), nitrogen dioxide ( $\text{NO}_2$ ), and nitric acid ( $\text{HNO}_3$ ).

Vertical  $\text{SO}_2$  profiles (Fig. 1) from the MIPAS  $\text{SO}_2$  single profile retrieval (Höpfner et al., 2015) were used to identify plumes of volcanic eruptions. We utilized a gridded dataset from these retrievals with a three-dimensional sampling of  $60^\circ$  longitude,  $10^\circ$  latitude, and 1 km altitude with a vertical coverage of 10 to 23 km and a temporal averaging of 5 d. The lower-altitude limit varies with the tops of clouds in the troposphere, especially in tropical regions.

The typical random uncertainty for a single measurement of a volume mixing ratio profile is estimated to be 70–100 pptv. For the gridded dataset used here, systematic uncertainties are more important. These were estimated to be 10–75 pptv (10%–180%) under background conditions of the upper troposphere/lower stratosphere (UTLS) and 10–110 pptv (10%–75%) under volcanic influence (Höpfner et al., 2015).

### 2.2 GOMOS

The GOMOS instrument on ENVISAT operates based on the principle of stellar occultation. GOMOS provides data on stratospheric aerosol extinction as well as  $\text{O}_3$ ,  $\text{NO}_2$ , nitrogen trioxide ( $\text{NO}_3$ ) and air density (Kyrölä et al., 2010). The principle of stellar occultation is described in detail in Bertaux et al. (2010). In short, this self-calibrating sounding method scans the atmosphere by pointing to a star during its set or rise. The measured spectra vary with the tangent altitude due to the absorption and scattering of light by the different atmospheric species along the line of sight.

In a first step, the GOMOS inversion algorithm determines the slant column density of gaseous species and the slant aerosol optical depth along the optical path (Vanhellemont et al., 2004). This process makes use of reference absorption spectra of the main absorbing species, such as the ones provided by the MPI-Mainz UV/VIS Spectral Atlas of Gaseous Molecules of Atmospheric Interest (<https://www.uv-vis-spectral-atlas-mainz.org/uvvis/>, last access: 10 January 2023) and extinction cross-section values representative for aerosols. Also, it requires the removal of the contribution of Rayleigh scattering by neutral air, which has to be carefully estimated, because satellite measurements cannot discriminate the contributions of neutral air density and very small particles compared to the wavelength (e.g. new particles arising from the conversion of  $\text{SO}_2$  to fresh aerosol particles), respectively. In a second step, vertical density profiles of the target gas species and vertical profiles of the aerosol

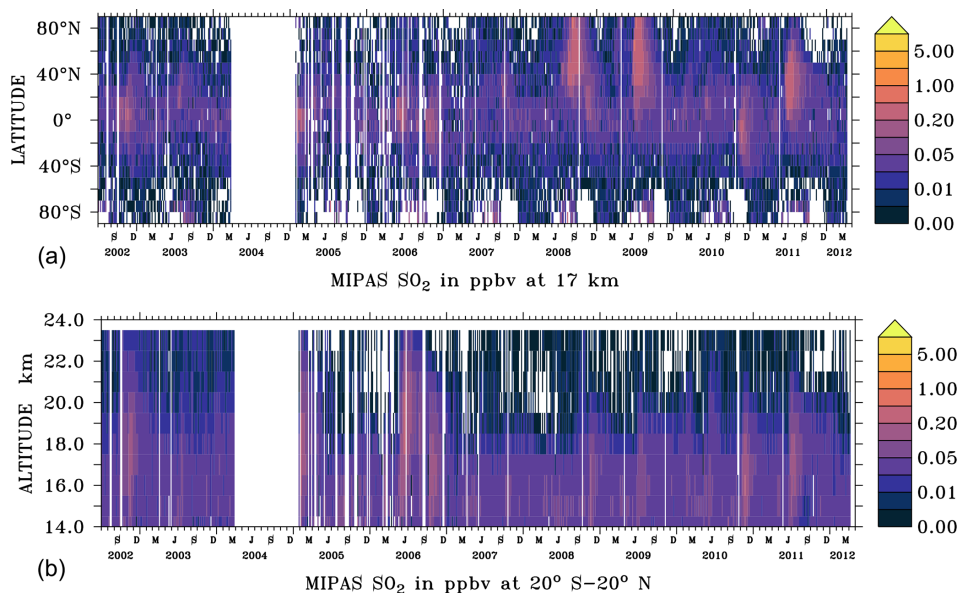


**Figure 1.** The volume mixing ratios of SO<sub>2</sub> in ppbv as derived from the MIPAS instrument (Höpfner et al., 2015). The dataset spans the period 1 July 2002–8 April 2012 (5 d averages). Horizontal distribution at 17 km altitude (a) and vertical distribution for tropical regions 20° S–20° N (b). White: no data.

extinction coefficient are obtained from the slant quantities (Bertaux et al., 2010).

GOMOS uses four spectrometers providing measurements at wavelengths from the UV-visible range to the near-IR range in four spectral regions: 248–371, 387–693, 750–776, and 915–956 nm (Robert et al., 2016). As the original inversion algorithm (the operational algorithm IPF – Instrument Processor Facility) was poorly effective for the retrieval of the aerosol extinction coefficient and only one extinction channel was obtained at the reference wavelength of 550 nm (Vanhellemont et al., 2010), a new retrieval algorithm called AerGOM was designed (Vanhellemont et al., 2016; Robert et al., 2016) in order to improve the spectral inversion. The main changes brought to AerGOM concern a change in the retrieval strategy where all atmospheric contributions are retrieved all together instead of one by one, a revision of the parametrization of the aerosol spectral dependence, and a more accurate estimate of the scattering cross section by air. Also, the cross-section spectra for the gaseous species were revised using up-to-date reference spectra (Bingen et al., 2019). AerGOM provides the spectral dependence of the aerosol extinction coefficient between about 350 and 750 nm.

The typical extinction uncertainty exhibits large variability as a function of the star parameters (from about 5 %–15 % in the most favourable cases of bright, hot stars to about 40 %–70 % in the less favourable cases of dim, cold stars) (Bingen et al., 2017). A full validation of AerGOM, version 1.0, is presented by Vanhellemont et al. (2016). The main factor influencing the uncertainty is the weakness of the star signal, which is alleviated by the high measurement rate made

possible by the abundance of stars. The large variability in the magnitude and temperature of the occultated stars also significantly influences the measurement uncertainty (Robert et al., 2016).

From AerGOM, climate data records were processed for use in chemistry-climate models (Bingen et al., 2017), and these are the datasets used in the present study. Figures 2 and 3 show the aerosol extinction from the GOMOS instrument at wavelengths of 550 nm (Fig. 2) and 750 nm (Fig. 3), respectively. In both cases, a gridded aerosol extinction dataset is used (CCI-GOMOS dataset in version 3.00; see Bingen et al., 2017).

The resolution of the CCI-GOMOS dataset was optimized to a grid of 5° latitude by 60° longitude and a time resolution of 5 d. This choice is made possible by the high measurement rate and is more suitable for describing the aerosol distribution than zonal monthly means, because it allows detection of the signature of aerosol patterns with a lifetime of as short as a week (e.g. medium-sized volcanic eruptions).

### 2.3 Optical Spectrograph and InfraRed Imaging System (OSIRIS)

The dataset from OSIRIS allowed us to extend the time series beyond April 2012, after which the signal of the ENVISAT satellite was lost. OSIRIS is a limb scatter instrument, which was launched on board the Odin satellite on 20 February 2001 and is still operating today.

OSIRIS performs limb scans of atmospheric radiance spectra at wavelengths from the UV to near-IR ranges (274–810 nm) (Bourassa et al., 2012a). To obtain the vertical pro-

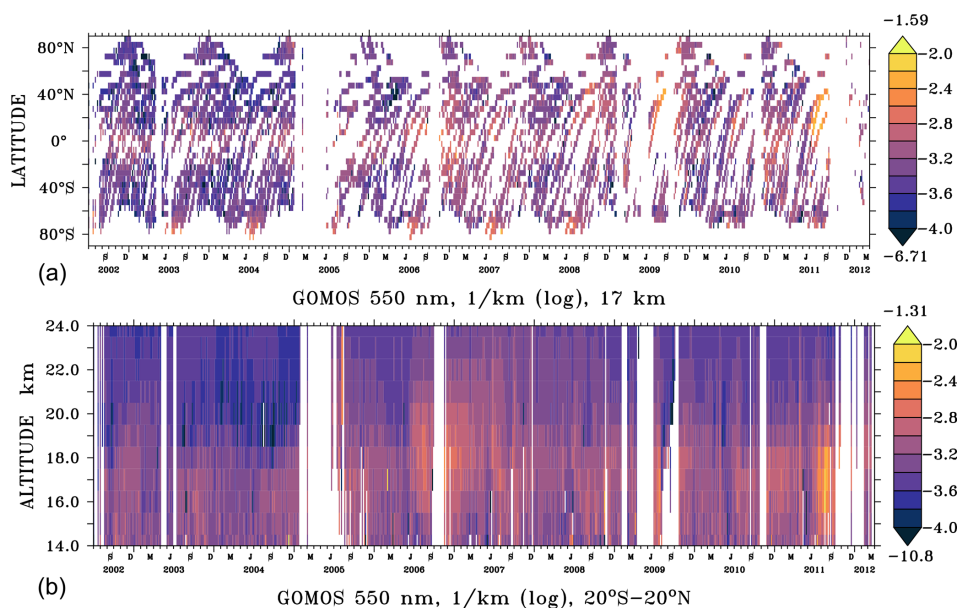


**Figure 2.** The decadal logarithm (log) of the aerosol extinction coefficient ( $\text{km}^{-1}$ ) as derived from the GOMOS instrument data v.3.00 at a 550 nm wavelength from Bingen et al. (2017). The dataset spans the period 15 April 2002–8 April 2012 (5 d averages). Horizontal distribution at 17 km altitude (a) and vertical distribution for tropical regions 20° S–20° N (b). Maximum and minimum values appear above (yellow) and below (dark blue) the colour keys, respectively. White: no data.

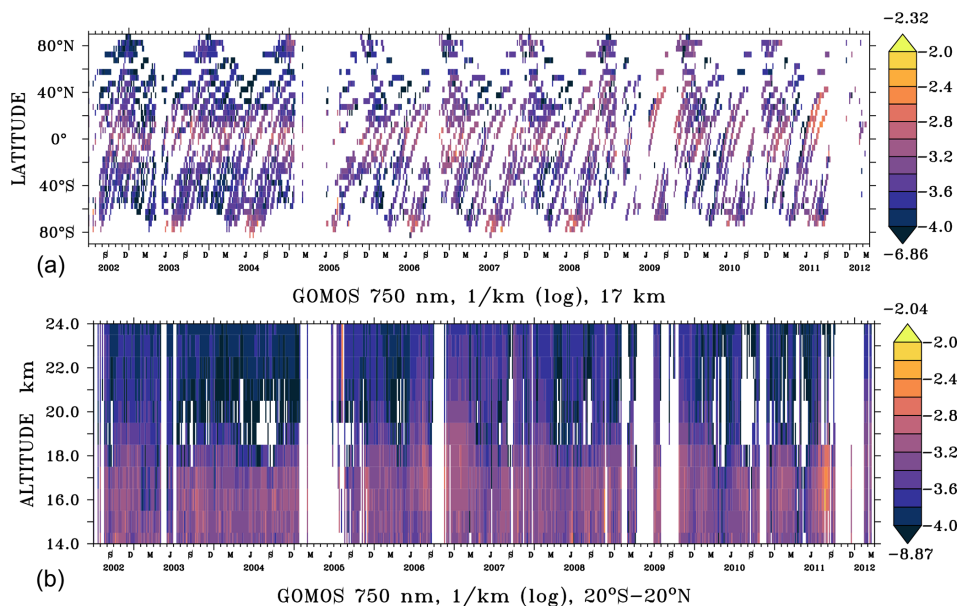


**Figure 3.** Like Fig. 2 but for the 750 nm wavelength.

files of aerosol extinction at altitudes from 10 to 35 km (Rieger et al., 2015), the aerosol scattering properties are calculated with a refractive index of  $1.427 + i7.167 \times 10^{-8}$  using Mie theory at 750 nm wavelength and a sulfate concentration of 75 %  $\text{H}_2\text{SO}_4$  and 25 %  $\text{H}_2\text{O}$  (Rieger et al., 2018).

For this study, the OSIRIS version 5.10 aerosol retrieval was used until October 2017 and version 7.1a afterwards (for details, see Rieger et al., 2019; Bourassa et al., 2012a).

OSIRIS provides coverage from 82° S to 82° N over the course of the year. Extinction is retrieved where the tangent point is illuminated, which is primarily in the summer hemisphere (see Fig. 4). The grid resolution is 1 km altitude, 5° latitude, and 30° longitude with 5 d-averaged time intervals.

The total uncertainty is about 10 %–15 % in the aerosol layer between 15 and 30 km, where the sensitivity of the measurements decreases with increasing optical depth. Due

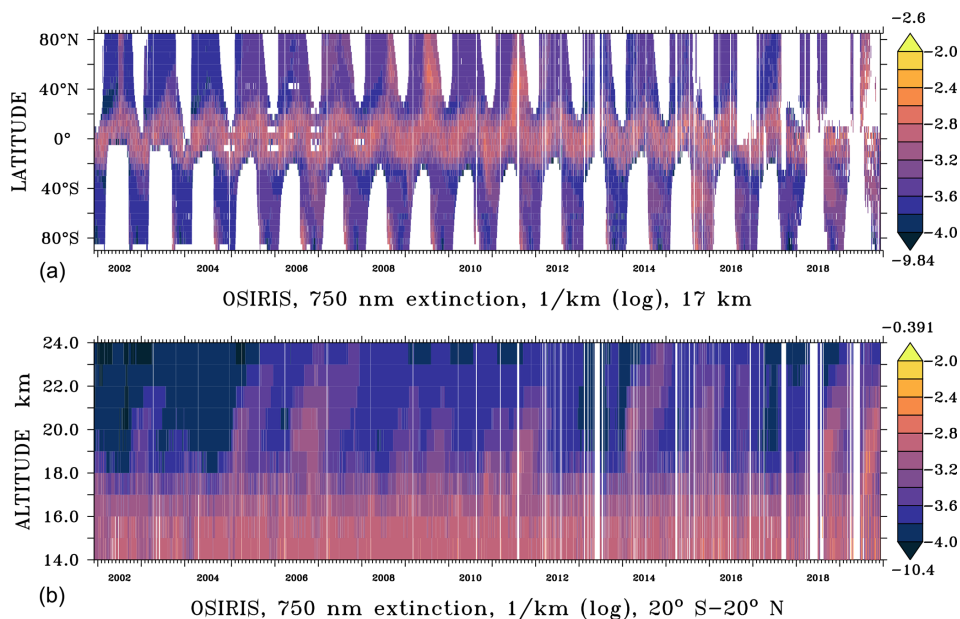


**Figure 4.** The logarithm  $\log(\text{km}^{-1})$  of the aerosol extinction as derived from the OSIRIS instrument at a 750 nm wavelength by Bourassa et al. (2012a) and Rieger et al. (2019). The dataset spans the period 1 December 2001–December 2019 (5 d averages). Horizontal distribution at 16.5 km altitude (a) and vertical distribution for tropical regions 20° S–20° N (b). Maximum and minimum values appear above (yellow) and below (dark blue) the colour keys, respectively. White: no data.

to measurement noise, the uncertainty dominates the signal above 30 km and in the troposphere (Rieger et al., 2015). At altitudes near and below the tropopause, the OSIRIS measurements are sensitive to clouds that may be interpreted as elevated aerosols. This is likely contributing to the larger background extinction values measured below approximately 17 km in the tropics, as can be seen in Fig. 4 (bottom), and the uncertainty is higher.

#### 2.4 Stratospheric Aerosol and Gas Experiment II (SAGE II)

SAGE II was a solar occultation instrument that performed measurements during sunrise and sunset. The SAGE II aerosol extinction measurements on board the Earth Radiation Budget Satellite (ERBS) started in October 1984 and ended in August 2005. This dataset is important for the model set-up before the ENVISAT period starting in 2002. The gridded aerosol extinction is derived from the V7.00 Level2 profiles provided by the Earth Observing System Data and Information System of NASA (EOSDIS) database (Fig. 5).

The gridded SAGE II dataset used in the present study provides a near-global coverage with latitudes between 80° N and 80° S, with a horizontal grid resolution of 60° in longitude and 10° in latitude and a vertical resolution of 0.5 km between 13 and 30 km altitude. SAGE II measured in occultation; thus, its measuring principle is similar to that of GOMOS. The two main differences between GOMOS and

SAGE II are that the latter used the sun as a light source, which results in a much better signal-to-noise ratio. On the other hand, its measurement rate is much lower than that of GOMOS, since only two measurements (one sunrise and one sunset) are possible per orbit, so that a near-global coverage is achieved in about 1 month.

Measurements occur at seven wavelengths between 386 and 1020 nm. The vertical profiles of O<sub>3</sub>, NO<sub>2</sub>, and water vapour are provided as well as aerosol extinction coefficients at four wavelengths (386, 452, 525, and 1020 nm) from the middle troposphere to the upper stratosphere.

After the large eruption of Mount Pinatubo in 1991, “saturation” effects at lower altitudes were observed in the profiles for more than 1 year, meaning that the aerosol load was so high that the light signal received by the instrument was below the limit of detection. This effect corresponds to the large white areas for 1991 and 1992 in Fig. 5. Red pixels around 14–16 km correspond to measurements contaminated by clouds, increasing the optical depth in the upper troposphere/lower stratosphere (UTLS) region in Fig. 5b. The perturbations by convective clouds occur mostly over the western Pacific and were excluded in the procedure for estimating the SO<sub>2</sub> injections. The data gaps in the year 2000 were caused by an instrument failure causing SAGE II to be switched off for several months.

The uncertainty of the operational SAD (surface area density) product during background periods is affected by several parameters, including the lack of sensitivity to particles with radii smaller than 100 nm, the number of degrees of

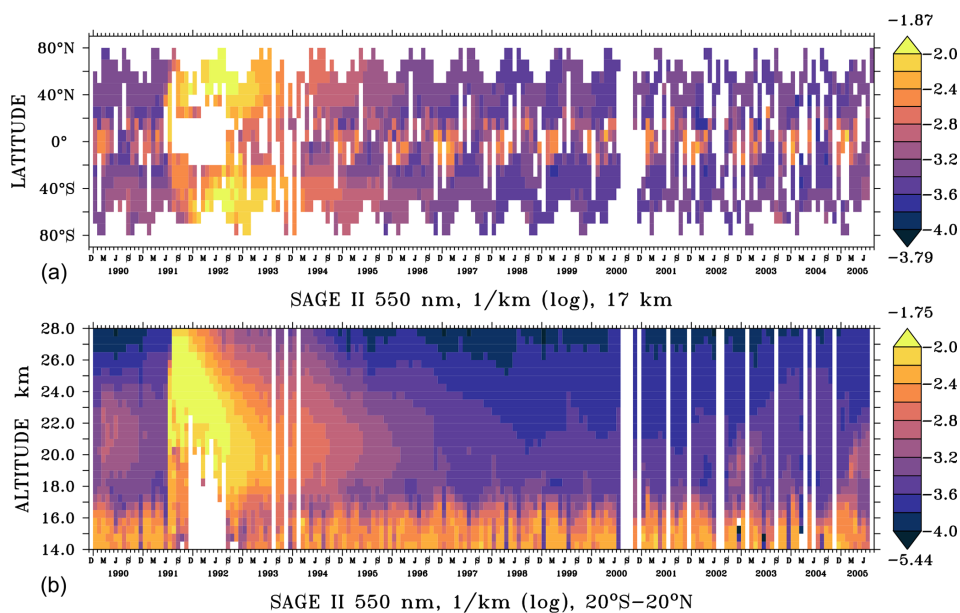


**Figure 5.** The logarithm of the extinction coefficient ( $\text{km}^{-1}$ ) of the SAGE II instrument from Thomason et al. (2008). The dataset spans the period January 1990–August 2005 (monthly). Horizontal distribution at 16.75 km altitude (a) and vertical distribution for tropical regions  $20^{\circ}\text{S}$ – $20^{\circ}\text{N}$  (b). Maximum and minimum values appear above (yellow) and below (dark blue) the colour keys, respectively. White: no data.

freedom indicated by the averaging kernels of the aerosol extinction at different wavelength channels, and the temperature profile used in the data processing (Thomason et al., 2008).

### 3 Description of the set-up for the EMAC model

The simulations in this study were performed with EMAC (ECHAM5/MESSy Atmospheric Chemistry), a coupled atmospheric circulation model consisting of the 5th generation of the European Centre Hamburg general circulation model (ECHAM5) (Roeckner et al., 2003, 2006) and the Modular Earth Submodel System (MESSy) (Jöckel et al., 2005, 2006, 2010).

The model simulations performed by Bingen et al. (2017) and Brühl et al. (2018) in the period from 2002 to 2012 were extended in this study to 1990 to 2019. For these model simulations, a higher horizontal resolution T63 ( $1.87^{\circ} \times 1.87^{\circ}$ ), instead of T42 ( $2.81^{\circ} \times 2.81^{\circ}$ ) in Bingen et al. (2017), was chosen. As we focus on the stratosphere, the middle atmosphere version L90 with 90 layers up to 0.01 hPa ( $\sim 80$  km) and a high vertical resolution in the lower stratosphere was needed (Giorgetta et al., 2006). The temperature and the dynamics above the boundary layer are nudged to the meteorological ERA-Interim reanalysis data of the European Centre for Medium-Range Weather Forecasts (ECMWF) up to about 100 hPa, while the sea surface temperatures (SSTs) and sea ice are prescribed using ECMWF data (more details in Jöckel et al., 2006).

As EMAC is a very complex chemistry-climate model, it contains many sub-models and functions which are essential for running the simulations but which are not directly related to the sulfur cycle; these are mentioned in Appendix A. In this section we focus on the sulfur cycle and aerosol.

The plumes of outgassing volcanic  $\text{SO}_2$  emissions (Diehl et al., 2012) are imported via the OFFEMIS sub-model as three-dimensional field volume emission fluxes (Kerkweg et al., 2006b). The exchange of DMS between the air–sea interface of the ocean and the atmosphere is simulated by the AIRSEA sub-model (Pozzer et al., 2006).

The gas- and aqueous-phase chemistry in the troposphere and stratosphere is calculated interactively with the CAABA/MECCA (Chemistry As A Boxmodel Application/Module Efficiently Calculating the Chemistry of the Atmosphere) sub-model (Sander et al., 2011). Specifically, the chemically generated  $\text{SO}_2$  is calculated from fluxes of sulfate precursor gases and further transformed to  $\text{H}_2\text{SO}_4$  (Brühl et al., 2018), together with the emitted  $\text{SO}_2$ . OH and ozone are fully interactive. CAABA/MECCA is also coupled to the Multiphase Stratospheric Box Model (MSBM) for heterogeneous reactions on sulfate aerosols and Polar Stratospheric Clouds (PSCs) (Jöckel et al., 2010) to allow for feedback on ozone. The uptake and oxidation of tracers is considered by the SCAVENGING sub-model for both liquid- and mixed-phase clouds (Tost et al., 2006a), also including the aqueous sulfur oxidation of  $\text{SO}_2$  to  $\text{SO}_4^{2-}$ .

For parametrization of aerosol microphysical processes, we used the Global Modal-aerosol eXtension (GMXe) aerosol module (Kerkweg, 2005; Stier et al., 2005;

Vignati et al., 2004), and we described aerosol species using four soluble and three insoluble interacting log-normal aerosol modes. The original mode boundaries of the aerosol size distribution from Pringle et al. (2010) were adapted for this set-up to volcanic aerosol conditions in the stratosphere as shown in Table 1 to avoid overly rapid sedimentation of coarse aerosol particles after big volcanic eruptions. The nucleation of new particles consists only of completely soluble sulfate aerosols and is calculated by the parametrization used by Vehkamäki et al. (2002). Further, the evaporation of liquid sulfate particles back to the gas phase in the middle stratosphere is possible in the model.

The AEROSOL OPTICAL properties in the model are calculated online with the AEROPT sub-model (Dietmüller et al., 2016) and are coupled to the GMXe sub-model. The resulting extinction coefficient is given at wavelengths of 350, 550, 750, and 1025 nm for comparison with GOMOS, OSIRIS, and SAGE. Finally, the aerosol optical properties like wavelength-dependent particle extinction cross section, single scattering albedo, and asymmetry parameter for each aerosol mode from AEROPT (Dietmüller et al., 2016) are used in the radiation scheme as input for the radiative transfer calculations and to calculate the AOD. The influence of stratospheric aerosol on instantaneous radiative forcing and heating is calculated online for diagnostic purposes (for details, see Dietmüller et al., 2016). Via multiple calls of the RAD sub-model in one simulation, these quantities are calculated online from the difference of fluxes or heating rates for the cases with stratospheric aerosol above the calculated tropopause (in earlier studies only above 100 hPa) and without any aerosol (Brühl et al., 2015), additionally to the call with full aerosol used for the interaction with dynamics.

It is not possible to separate volcanic aerosol from the background in these model simulations.

#### 4 Volcanic Sulfur Emission Inventory

In a previous inventory of volcanic eruptions based on SO<sub>2</sub> vertical profiles from MIPAS, the aerosol instantaneous radiative forcing from 2002 to 2011 was estimated by simulating the evolution of SO<sub>2</sub> in the atmosphere reported by Brühl et al. (2015) and by improving the resulting time series using aerosol measurements from Bingen et al. (2017). The results of these simulations showed that significant discrepancies remained with respect to radiative forcing estimated from measurements (Brühl et al., 2018).

In this work, we further improve the volcanic sulfur emission inventory by analysing additional satellite datasets (Sect. 2) and by including all identified relevant eruptions between 1990 and 2019. To derive the volcanic three-dimensional SO<sub>2</sub> perturbation from MIPAS, we normally select the 5 d interval at the time of the eruption and the following one. For medium-sized eruptions, up to six consecutive intervals are used to correct for saturation effects or artifacts

from the applied cloud clearing scheme in the case of ash (Höpfner et al., 2015). A background of about 10 pptv, the typical value originating from OCS oxidation, is subtracted. In some cases this value can be larger because of remnants of a previous volcanic event. For MIPAS, corrections of the order of up to 30 % were sometimes necessary because of gaps (containing zero values) to be consistent with the total injected SO<sub>2</sub> mass derived from the MLS (Microwave Limb Sounder) or OMI (Ozone Monitoring Instrument). Here the corrected values serve as a reference for SO<sub>2</sub> derived from the instruments measuring extinction.

The GOMOS dataset is very important for compensating for data missing from the MIPAS instrument (Sect. 2.1), where several important eruptions in 2004 and 2006 could not be identified (Bingen et al., 2017). An appropriate comparison of SO<sub>2</sub> mixing ratio measurements from MIPAS and of the aerosol extinction from GOMOS requires consideration of a time shift of 1 to 2 weeks as a result of the particle formation from the gas phase. We typically select a 10 d period beginning about a week after an eruption in the tropics. For higher latitudes the selected period is later and longer, taking into account the longer conversion time (due to less OH). The SO<sub>2</sub> mixing ratio perturbation  $\Delta\text{VMR}$  is derived from the extinction perturbation  $\Delta\beta_{\text{ext}}$  (750 nm) as in Eq. (1) using a constant ratio between model-calculated sulfate concentration and its share in the extinction in the lower stratosphere of low latitudes:

$$\Delta\text{VMR} = 1.2 \times 10^{12} \frac{\Delta\beta_{\text{ext}}}{\rho} f. \quad (1)$$

$\rho$  is the altitude-dependent air density (molec. cm<sup>-3</sup>) and  $f$  an empirical factor which equals 1 for sufficient data coverage (for examples and more details, see Appendix B). We assume that the spatial patterns of the perturbation of extinction and sulfate are the same as for SO<sub>2</sub>. A similar technique is used for OSIRIS and can be used for SAGE II data.

If data gaps cause a shift of the time period away from the maximum perturbation or a low bias in the zonal average due to the zero values in the gaps at some longitude bin or in a period, a correction factor  $f > 1$  based on comparison of total injected SO<sub>2</sub> mass with the one taken from other satellite data is applied in Eq. (1). Correction factors up to 2 have to be applied in some cases because of data gaps, incomplete profiles (both containing zero values), or high latitudes (for examples, see Appendix B). An extreme case is the eruption of Calbuco, with a correction factor of 3 for removal processes, because of a shift of 3 months due to a big data gap. To estimate the factor in this “worst” case, we iterated calculated extinctions to agree with OSIRIS and also used observations and assumptions by Vernier et al. (2016) like the decay of extinction by sulfate with time over 4 months.

On the other hand, the factor can be as small as 0.5 to account manually for sulfate remnants of eruptions occurring 2–4 weeks before the date of the eruption to be analysed or for cloud perturbations. The factors  $f$ , together with the used

**Table 1.** Diameters of aerosol-mode boundaries in the GMXe sub-model for tropospheric (Pringle et al., 2010) and volcanic stratosphere conditions (Brühl et al., 2018), including the corresponding mode distribution width ( $\sigma$ ).

Mode boundaries	Pringle et al. (2010)	$\sigma$	Brühl et al. (2018)	$\sigma$
Nucleation mode: soluble	< 10 nm	1.69	1–12 nm	1.59
Aitken modes: soluble and insoluble	10–100 nm	1.69	12–140 nm	1.59
Accumulation modes: soluble and insoluble	100 nm–1 $\mu$ m	1.69	140 nm–3.2 $\mu$ m	1.49
Coarse modes: soluble and insoluble	> 1 $\mu$ m	2.2	> 3.2 $\mu$ m	1.7

time periods, are provided in the Supplement (Table S1 for OSIRIS and Table S2 for GOMOS).

SO<sub>2</sub> column data from the OMI, Total Ozone Mapping Spectrometer (TOMS), Ozone Mapping and Profiler Suite (OMPS), and other nadir instruments were used to verify the consistency of the data and to fill in data gaps, marked as white areas in all satellite images. Especially in 2018 and 2019 the OSIRIS data are so sparse that constraints from instruments like OMPS-LP (Zawada et al., 2018) or analogous events of previous years have to be superimposed for some eruptions. These eruptions are marked with “T” in Table 2. For the marked events in 2006 and 2007 data from OMI helped to identify them because of sparse MIPAS and GOMOS data.

For SAGE II in most cases the SO<sub>2</sub> mixing ratio is derived using the parametrization of Grainger et al. (1995) which converts SAD to volume density as a first step. We use pressure and temperature provided to convert from mass density to a volume mixing ratio, assuming that observed sulfate is produced from injected SO<sub>2</sub> some weeks ago. With this method it is easier to correct for cloud contamination than by using the extinction directly as above for the other instruments.

Case studies for three events, comparing SO<sub>2</sub> results from the different satellites and the different conversion methods, are presented in Appendix B.

The amount of sulfur emitted by each eruption is calculated by integration over the three-dimensional SO<sub>2</sub> perturbation plumes, excluding tropospheric emissions below 12 km at high latitudes, 13 km at mid latitudes, and 14 km at low latitudes. The latter is selected to include possible convective transport from the upper troposphere into the stratosphere in the tropics. The limits at the mid and high latitudes above the mean tropopause were selected to exclude cloud perturbations by frontal systems or uncertain satellite data. This can lead to an underestimate of injected mass in some cases. The plumes do not cover the whole globe: they are always in a latitude range derived manually from the satellite data. In the case of multiple events the integration over the perturbed area is split considering the mean wind and consistency with nadir observations for fine-tuning of the latitude and longitude boundaries. An example is shown in Appendix B.

Geological information and additional observations of plume heights were received from the Global Volcanism Pro-

gram, Smithsonian Institute (<https://volcano.si.edu/>, last access: 10 January 2023). Their reports several times indicate that even VEI 2 eruptions (volcanic explosivity index) can reach the upper troposphere (or lower stratosphere, which confirms the satellite observations).

The resulting volcanic emission inventory is presented in Table 2 and provides the injection time into the model, the coordinates of the ejected plume, and the amount of emitted SO<sub>2</sub>. Each volcano is identified by its name if available or by the concerned region if the name is unknown. The altitudes and latitudes indicated in the table correspond to the locations of the maximum SO<sub>2</sub> mixing ratios of the volcanic plumes. The longitudes refer to the locations of the volcanoes, because the plumes have been moved by the zonal winds during the time lag between eruption and observation. In the cases of OSIRIS, SAGE, and GOMOS this shift can easily be 100°. The entries in the table might be used for a point source approach.

It should be noted that the date of the volcanic eruption can differ by a few days from the date of injection in the model simulation, because the temporal resolution of the datasets is 5 d (or weeks in the SAGE period). In a lot of cases, more than one eruption is found in the same 5 d interval. In such a case, all eruptions are listed on the same line. Several times the used time period for extraction has to be extended because of data gaps, which increases the uncertainty and complicates the identification of the right volcano. In such a case, the name of the most probable volcano is tagged with “?”. If the SO<sub>2</sub> emissions of two volcanoes cannot be separated with certainty, both are indicated with a “+” on the same line. This uncertainty is frequent in the Republic of Vanuatu, an island country located in one of the most volcanically active regions in the South Pacific, referred to as “Vanuatu” in Table 2.

When comparing the SO<sub>2</sub> emissions reported here with those of Carn et al. (2016), it should be noted that Carn et al. (2016) make use of total SO<sub>2</sub> emissions, including rapidly removed tropospheric SO<sub>2</sub>, while the present study only takes into account the long-lived, climate-relevant stratospheric fraction of the emitted SO<sub>2</sub>. A comparison to Carn et al. (2016) and Mills et al. (2016) of the injected volcanic SO<sub>2</sub> masses per year is presented in Appendix C2.

**Table 2.** Inventory of volcanic SO<sub>2</sub> emissions into the stratosphere integrated over latitude belts above 14 km at low latitudes, 13 km at mid latitudes and 12 km at high latitudes from the three-dimensional mixing ratio perturbations. Listed altitudes and latitudes represent the region of maximum mixing ratio perturbation, and the altitudes are close to the top injection height. For some eruptions, two plumes at different altitudes were identified, and the listed mass is the sum – derived from satellite data (2002–2012) by MIPAS (M) and GOMOS (G) and based on a previous study by Brühl et al. (2018) with scaling factors for T63 and already published in an earlier version in Bingen et al. (2017) (*volcano names in italic*). Extended with satellite data from SAGE II(V7.00) (S) back to 1990–2002 and from 2012 to 2019 by OSIRIS (O). Sometimes TOMS/OMI/OMPS (T) are also used for handling data gaps. For a detailed description, see the text. Data available online as a Fortran-formatted ASCII table and the three-dimensional data as netcdf ([https://doi.org/10.26050/WDCC/SSIRC\\_3](https://doi.org/10.26050/WDCC/SSIRC_3), Brühl et al., 2021).

Volcano or region	Time	Latitude (°)	Longitude (°)	Altitude (km)	SO <sub>2</sub> (kt)	Instrument
Kelut	11 Feb 1990	−8	112	16, 22	410	S
Gamalama	25 Apr 1990	0	127	16	96	S
Raung (?)	25 Jul 1990	−8	115	16	63	S
Pacaya + Sabancaya	16 Sep 1990	15	−90	16	10	S
	6 Oct 1990	−16	−72	17	75	S
Papua + Fernandina	12 Jan 1991	−4	145	17	88	S
	20 Apr 1991	0	−92	16	118	S
Pinatubo	16 Jun 1991	15	120	23	16942	S
Hudson	10 Aug 1991	−46	−73	18	1276	S
Cerro Negro	10 Apr 1992	12	−87	22	18	S
Spurr	28 Jun 1992	61	−152	17	291	S
Spurr	19 Aug 1992	61	−152	16, 18	298	S
Spurr	18 Sep 1992	61	−152	17	187	S
Lascar	18 Apr 1993	−23	−68	22	376	S
Langila, Galeras (?)	30 Oct 1993	−5, 1	145, −70	17	50	S
Yasur?	17 Mar 1994	−16	165	16	80	S
Rinjani, Nyamuragira, Central America	6 Jul 1994	−8, −1, 12	117, 30, −90	16	63	S
Rabaul	20 Sep 1994	−4	150	18, 22	89	S
Merapi, Ecuador	23 Nov 1994	−7, 1	110, −70	17, 17	48, 57	S
Peru, Africa, Vanuatu	15 Feb 1995	−15, −1, −15	−78, 30, 168	17, 16, 16	7, 43, 25	S
Mexico + Soufriere Hills	10 Aug 1995	16	−98, −62	16	81	S
Peru + Colombia, Rabaul	10 Feb 1996	−15, 5, −4	−80, −80, 150	17, 16, 16	65, 96	S
Soufriere Hills	26 May 1996	16	−62	16	53	S
Soufriere Hills + Mexico, Rabaul	18 Sep 1996	16, −4	−62, −98, 150	16, 16	59, 28	S
Nyamuragira, Manam	3 Dec 1996	−1, −5	30, 145	17, 17	45, 90	S
Manam + Langila	11 Feb 1997	−5	145	17	107	S
Popocatepetl	1 Jul 1997	19	−98	16	32	S
Soufriere Hills, Philippines	20 Oct 1997	16, 16	−62, 121	15, 16	36, 20	S
Soufriere Hills, Papua	26 Dec 1997	16, −8	−62, 150	16, 16	37, 22	S
Tungurahua (?), Vanuatu	2 Feb 1998	−1, −16	−78, 168	17, 16	98, 15	S
Soufriere Hills	4 Jul 1998	16	−62	16	56	S
Manam, Cerro Azul, Nyamuragira	7 Oct 1998	−5, 0, −1	144, −90, 30	17, 17, 16	28, 39, 19	S
Guagua Pinch + Tungurahua, Vanuatu	23 Jan 1999	−1, −16	−78, 165	17, 16	75, 49	S
Cameroon	31 Mar 1999	4	10	16	63	S
Mayon, Colombia	22 Jun 1999	13, 2	124, −80	17, 16	41, 46	S
Soufriere Hills +	24 Jul 1999	16	−62	17	42	S
Ulawun, Tungurahua + Guagua Pichincha	16 Nov 1999	−5, −1	150, −78	17	31, 51	S

Table 2. Continued.

Volcano or region	Time	Latitude (°)	Longitude (°)	Altitude (km)	SO <sub>2</sub> (kt)	Instrument
Vanuatu, Nyamuragira, Tungurahua	4 Feb 2000	−16, −1, 0	165, 30, −78	17, 16, 16	33, 41, 12	S
Mayon + Vanuatu, Tungurahua	29 Feb 2000	13, −16, −1	124, 168, −78	16, 16, 16	25, 32	S
Ulawun (+ Miyakejima)	26 Sep 2000	−5	150	17	42	S
Nyamuragira, Mayon(?)	13 Feb 2001	−1, 13	30, 124	16, 18	47, 88	S
Ulawun	29 Apr 2001	−5	150	16	41	S
Mayon, Lopevi	23 Jun 2001	13, −16	124, 168	16, 16	49, 22	S
Tungurahua, Soufriere Hills	7 Aug 2001	0, 16	−78, −62	16, 16	29, 46	S
Africa, Tungurahua +	25 Sep 2001	−1, 0	30, −78	16, 16	31, 47	S
Tungurahua (+ Manam), Nyiragongo	14 Jan 2002	−1(−4), −1	−78(144), 30	17, 15	83, 19	S
Tungurahua (+ Africa)	20 Mar 2002	−1	−78 (30)	17	77	S
<i>Nyamuragira</i>	23 Jul 2002	−1	30	15	23	M
<i>Witori</i>	2 Aug 2002	−6	150	14	18	M
<i>Ruang</i>	26 Sep 2002	2	125	18	71	M, G
<i>El Reventador</i>	5 Nov 2002	0	−78	17	77	M, G
<i>Nyiragongo, Lokon</i>	9 Jan 2003	−1, 1	30, 125	15, 16	12, 10	M, G
<i>Nyiragongo, Lokon (Rabaul?)</i>	5 Mar 2003	−5, 1	30, 125	17, 15	12, 13	M, G
<i>Anatahan, Nyiragongo, Ulawun</i>	14 May 2003	16, −1, −5	143, 30, 150	16, 16, 17	9, 15, 6	M
<i>Lewotobi, Kanlaon</i>	13 Jun 2003	−8, 10	123, 123	15, 15	9, 15	M, G
<i>Soufriere Hills</i>	13 Jul 2003	16	−62	17	41	M, G
<i>Gamalama, Japan</i>	17 Aug 2003	1, 33	128, 131	16, 16	8, 7	M, G
<i>Bezmyianny or Klyuchevskoy</i>	6 Sep 2003	56	160	14	8	G
<i>Lokon, Soufriere Hills + Masaya</i>	26 Sep 2003	2, 15	125, −62	16, 16	7, 5	M, G
<i>Rabaul</i>	10 Nov 2003	−5	150	16	17	M, G
<i>Rabaul</i>	5 Dec 2003	−5	150	16	13	M, G
<i>Rabaul, Nyiragongo?</i>	9 Jan 2004	−5, −1	150, 30	17, 15	11, 9	M, G
<i>Langila, Nyiragongo?</i>	3 Feb 2004	−5, −1	150, 30	17, 17	11, 3	M, G
<i>Soufriere Hills</i>	4 Mar 2004	10	−62	17	22	M, G
<i>Nyamuragira, Awu + Tengger</i>	12 Jun 2004	−1, 4, −8	30, 125, 112	17, 15	20, 18	G
<i>Pacaya, Galeras</i>	17 Jul 2004	15, 1	−91, −77	17, 17	11, 11	G
<i>Galeras</i>	11 Aug 2004	1	−77	16	15	G
<i>Vanuatu, Rinjani + Kerinci</i>	30 Sep 2004	−16, −8, −2	168, 116, 101	15, 15, 17	7, 15	G
<i>Manam, Soputan</i>	30 Oct 2004	−4, 1	144, 125	16, 16	8, 11	G
<i>Manam, Nyiragongo</i>	24 Nov 2004	−4, −1	144, 30	17, 15	18, 11	G
<i>Nyiragongo, Reventador</i>	4 Dec 2004	0, 0	30, −77	16, 16	19, 5	G
<i>Vanuatu, Soputan</i>	24 Dec 2004	−16, 1	168, 125	17, 15	15, 16	G
<i>Manam</i>	28 Jan 2005	−4	144	18	130	M, G
<i>Anatahan (+)</i>	3 Apr 2005	16	143	15	15	M
<i>Anatahan, Soufriere Hills</i>	23 Apr 2005	16, 16	143, −62	16, 16	21, 21	M
<i>Anatahan, Fernadina, Vanuatu</i>	18 May 2005	16, 0, −16	143, −91, 168	15, 15, 15	8, 11, 6	M
<i>Anatahan, Santa Ana</i>	12 Jun 2005	16, 14	143, −90	15, 15	12, 9	M
<i>Anatahan, Soufriere Hills</i>	12 Jul 2005	16, 16	143, −62	15, 15	14, 10	M
<i>Anatahan, Raung</i>	6 Aug 2005	16, −8	143, 113	15, 15	13, 20	M
<i>Anatahan, Raung</i>	16 Aug 2005	16, −8	143, 113	15, 15	14, 17	M, G
<i>Santa Ana</i>	5 Oct 2005	14	−90	17	32	M
<i>Sierra Negra, Dabbahu</i>	25 Oct 2005	−1, −13	−91, 40	15, 15	16, 22	G
<i>Karthala, Galeras</i>	24 Nov 2005	−10, −2	43, −80	16, 16	13, 11	M, G
<i>Soputan, Lopevi</i>	24 Dec 2005	1, −16	125, 168	16, 16	23, 13	M, G

Table 2. Continued.

Volcano or region	Time	Latitude (°)	Longitude (°)	Altitude (km)	SO <sub>2</sub> (kt)	Instrument
<i>Rabaul +</i>	23 Jan 2006	−5	152	16	25	G
<i>Manam, Chile</i>	4 Mar 2006	−5, −40	144, −70	17, 16	58, 6	G, M, T
<i>Cleveland</i>	14 Mar 2006	53	−170	13	8	G, M
<i>Ecuador, Tinakula, Lascar</i>	18 Apr 2006	−5, −10, −23	−78, 166, −68	17, 17, 17	13, 17, 3	M
<i>Soufriere Hills</i>	23 May 2006	16	−62	19	125	M, G, T
<i>Kanlaon (+?)</i>	2 Jul 2006	10	123	20	42	M
<i>Tungurahua, Rabaul</i>	16 Aug 2006	−2, −4	−78, 150	19, 17	40, 20	M, G, T
<i>Rabaul</i>	10 Oct 2006	−4	150	17	131	M, T
<i>Ubinas, Vanuatu</i>	25 Oct 2006	−20, −20	−70, 168	17, 15	8, 25	M
<i>Ambrym</i>	9 Nov 2006	−10	160	17	27	M, T
<i>Nyamuragira, Mexico</i>	29 Nov 2006	5, 5	30, −90	17, 15	28, 21	M, G, T
<i>Bulusan, Sopotan, Vanuatu</i>	24 Dec 2006	13, 1, −16	125, 125, 168	18, 16, 15	8, 8, 14	M, G
<i>Karthala, Bulusan, Lascar, Shiveluch, Vanuatu</i>	23 Jan 2007	−10, 13, −23, 57, −16	43, 125, −68, 160, 168	17, 17, 15, 15, 15	5, 5, 6, 7, 5	M, G, T
<i>Nevado del Huila, Karthala, Vanuatu</i>	22 Feb 2007	0, −10, −16	−70, 43, 168	16, 15, 16	8, 10, 8	M, G, T
<i>Etna, Reventador, Ambrym</i>	24 Mar 2007	38, 0, −16	15, −78, 160	15, 16, 17	8, 17, 14	M, G, T
<i>Piton de la Fournaise, Reventador + Ulawun, Vanuatu, Nevado del Huila</i>	8 Apr 2007	−20, 0	57, −80	16, 16	22, 11	M, G, T
<i>Papua, Kamchatka, Nyamuragira, Ubinas + Lascar</i>	3 May 2007	−5, −25, 3	150, 160, −70	15, 15, 15	11, 5, 6	M, G, T
<i>Llaima, Vanuatu, Bulusan Sopotan, Bezymianny, Telica</i>	13 May 2007	−10, 50, 0, −20	150, 150, 30, −75	16, 16, 16, 16	6, 1, 10, 6	M, G
<i>Lengai, Mexico</i>	23 May 2007	−30, −15, 13	−70, 160, 125	18, 15, 17	10, 6, 7	M, G
<i>Raung, Japan (+)</i>	12 Jun 2007	1, 56, 13	125, 160, −87	16, 14, 15	13, 7, 9	M, G
<i>Manda Hararo, Java</i>	2 Jul 2007	2, 20	29, −90	16, 15	14, 9	M
<i>Vanuatu, Mexico</i>	27 Jul 2007	−5, 35	110, 130	15, 15	10, 10	M
<i>Jebel al Tair, Galeras</i>	11 Aug 2007	12, −5	40, 115	17, 15	13, 14	M, T
<i>Galeras, Jebel al Tair, Sopotan</i>	20 Sep 2007	−5, 20	180, −90	16, 16	8, 13	M
<i>Sopotan or Krakatau, Galeras, Chikurachki</i>	5 Oct 2007	16, 1	42, −80	16, 16	41, 8	M, T
<i>Talang, Galeras</i>	4 Nov 2007	−2, 15, −5	−80, 42, 110	16, 16, 16	7, 5, 8	M, G
<i>Ulawun?</i>	14 Nov 2007	−5, −1, 50	110, −75, 155	16, 16, 15	9, 8, 10	M
<i>Nevado del Huila, Llaima</i>	9 Dec 2007	0, 0	100, −75	16, 16	10, 12	M
<i>Galeras, Anatahan</i>	19 Dec 2007	1	150	17	17	M, G
<i>Tungurahua, Papua</i>	3 Jan 2008	1, −35	−75, −71	17, 15	26, 4	M
<i>Batu Tara (+)</i>	23 Jan 2008	−3, 15	−80, 145	16, 16	14, 7	M
<i>Lengai, Andes, Kerinic</i>	12 Feb 2008	−5, −5	−80, 155	16, 17	13, 10	M
<i>Egon, Nevado del Huila</i>	13 Mar 2008	−5	125	16	26	M, G
<i>Mexico, Ibu, Chaiten</i>	28 Mar 2008	−5, 5, −2	36, −80, 101	16, 16, 16	6, 4, 7	M
<i>Mexico, Barren Island, Chaiten</i>	12 Apr 2008	−5, 5	122, −76	15, 17	14, 9	M
<i>Sopotan, Nicaragua/Costa Rica</i>	27 Apr 2008	15, 1, −35	−90, 125, −70	16, 16, 16	9, 11, 3	M
<i>Okmok, Sopotan</i>	12 May 2008	10, 10, −35	−90, 90, −70	14, 16, 14	10, 14, 5	M
<i>Kasatochi</i>	16 Jun 2008	1, 1	125, −85	16, 16	26, 8	M
<i>Dallafilla, Nevado del Huila, Reventador</i>	21 Jul 2008	53, 1	−168, 125	16, 16	51, 27	M
<i>Karangetang, Galeras, Japan</i>	15 Aug 2008	52	−175	17	273	M, G
	13 Nov 2008	14, 3	40, −78	17, 17	39, 28	M
	18 Dec 2008	3, 0, 30	125, −80, 130	17, 17, 15	15, 10, 9	M, G

Table 2. Continued.

Volcano or region	Time	Latitude (°)	Longitude (°)	Altitude (km)	SO <sub>2</sub> (kt)	Instrument
<i>Barren Island, Galeras</i>	2 Jan 2009	10, 3	90, -80	17, 15	10, 10	M
<i>Indonesia?, Galeras</i>	27 Jan 2009	-5, 0	100, -80	16, 16	12, 10	M
<i>Galeras, Villarrica, Karangetang, Vanuatu</i>	16 Feb 2009	-2, -35, 3, -16	-78, -75, 100, 168	16, 15, 16, 17	11, 6, 6, 7	M
<i>Redoubt, Galeras</i>	28 Mar 2009	60, 0	-155, -75	13, 15	61, 43	M
<i>Fernandina, Nyamuragira</i>	12 Apr 2009	0, 0	-90, 30	16, 16	12, 16	M
<i>Galeras + Reventador</i>	7 May 2009	0	-75	15	25	M
<i>Rinjani, Vanuatu, Reventador</i>	22 May 2009	-5, -15, 3	116, 165, -80	16, 16, 16	4, 4, 13	M
<i>Sarychev, Manda Hararo (+?)</i>	21 Jun 2009	48, 12	153, 40	16, 16	446, 82	M, G
<i>Vanuatu, Mayon, Galeras</i>	4 Oct 2009	-15, 13, 2	165, 120, -80	17, 17, 17	4, 6, 10	M
<i>Tungurahua, Hawaii, Vanuatu</i>	19 Oct 2009	5, 20, -16	-76, -155, 165	16, 16, 16	7, 5, 5	M, G
<i>Galeras, Karkar, Vanuatu</i>	3 Dec 2009	0, -5, -16	-78, 146, 165	17, 17, 17	12, 10, 4	M
<i>Mayon, Nyamuragira, Vanuatu</i>	2 Jan 2010	13, 0, -15	120, 30, 168	16, 16, 16	8, 8, 9	M
<i>Turrialba, Vanuatu</i>	17 Jan 2010	5, -15	-82, 168	16, 16	9, 9	M
<i>Soufriere Hills</i>	16 Feb 2010	16	-62	17	36	M
<i>Arenal, Indonesia, Vanuatu</i>	2 Apr 2010	9, 0, -16	-84, 120, 168	15, 15, 15	14, 12, 5	M
<i>Tungurahua, Dukono, Vanuatu</i>	2 May 2010	-5, 2, -16	-78, 128, 168	16, 16, 16	14, 10, 7	M
<i>Pacaya, Ulawun, Sarigan</i>	6 Jun 2010	15, -5, 16	-91, 150, 145	17, 16, 15	27, 6, 4	M
<i>Ulawun, Costa Rica, Miyakejima</i>	16 Jul 2010	-5, 15, 35	150, -87, 140	16, 16, 16	8, 13, 6	M, G
<i>Karangetang, Nicaragua, Vanuatu</i>	15 Aug 2010	3, 15, -16	125, -85, 168	16, 16, 16	12, 12, 6	M
<i>Galeras, Sinabung</i>	30 Aug 2010	5, 5	-77, 100	16, 16	10, 12	M
<i>Karangetang, Barren Island</i>	4 Oct 2010	3, 12	125, 94	16, 16	20, 13	M
<i>Merapi</i>	8 Nov 2010	-7	110	17	97	M
<i>Tengger, Tungurahua, Chile</i>	23 Dec 2010	-8, -3, -40	110, -78, -75	17, 17, 17	16, 13, 8	M
<i>Tengger</i>	7 Jan 2011	-8	110	16	24	M
<i>Lokon, Planchon, Bulusan</i>	26 Feb 2011	1, -35, 13	125, -75, 125	16, 15, 16	13, 4, 12	M
<i>Karangtang, Sangay, Planchon</i>	23 Mar 2011	2, -2, -35	125, -78, -75	15, 15, 15	10, 10, 5	M
<i>Galeras?, Karangetang</i>	12 Apr 2011	5, 5	-77, 128	16, 16	10, 9	M
<i>Tungurahua, Dukono, Vanuatu</i>	2 May 2011	2, 2, -16	-78, 128, 160	16, 16, 15	13, 9, 5	M
<i>Grimsvötn, Lokon</i>	27 May 2011	65, 1	-20, 125	14, 16	18, 27	M
<i>Puyehue</i>	11 Jun 2011	-41	-71	13	23	G, M
<i>Nabro</i>	21 Jun 2011	13	41	18	406	M, G
<i>Soputan, Marapi</i>	20 Aug 2011	1, 0	125, 100	18, 16	9, 3	M, G
<i>Manam, Tungurahua</i>	19 Oct 2011	-4, -3	144, -78	16, 16	8, 8	M
<i>Nyamuragira</i>	18 Nov 2011	-2	29	16	31	M
<i>Gamalama, Nyamuragira</i>	18 Dec 2011	1, -1	128, 29	16, 15	19, 13	M
<i>Vanuatu, Nyamuragira</i>	12 Jan 2012	-16, -1	168, 29	16, 14	14, 12	M
<i>Vanuatu, Nyamuragira</i>	11 Feb 2012	-16, -1	168, 29	17, 17	16, 15	M
<i>Nevado del Ruiz, Marapi</i>	12 Mar 2012	-3, 0	-76, 100	16, 17	12, 15	M
<i>Nyamuragira, Mexico</i>	7 Jun 2012	-1, 20	29, -95	16, 15	30, 4	O
<i>Soputan, Nevado del Ruiz, Mexico</i>	27 Aug 2012	1, 5, 20	124, -76, -95	16, 16, 15	30, 15, 5	O
<i>Nyamuragira, Mexico, Peru</i>	14 Oct 2012	-1, 20, -20	29, -95, -70	16, 16, 15	40, 15, 10	O
<i>Nyamuragira, Paluweh, Nevado del Ruiz</i>	7 Nov 2012	-1, -8, 5	29, 122, -76	15, 16, 17	20, 30, 17	O
<i>Copahue, Lokon +</i>	22 Dec 2012	-38, 1	-71, 125	15, 17	10, 45	O
<i>Paluweh, Karkar</i>	3 Feb 2013	-8, -5	122, 145	16, 17	25, 22	O
<i>Karkar, Vanuatu (+?)</i>	10 Mar 2013	-5, -16	145, 168	17, 16	24, 20	O
<i>Rabaul, Nevado del Ruiz, Nyamuragira</i>	18 Apr 2013	-3, 5, -1	150, -76, 29	17, 17, 16	40, 9, 20	O
<i>Mayon, Turrialba, Pavlof</i>	8 May 2013	13, 10, 55	124, -84, -162	17, 16, 14	35, 24, 6	O
<i>Rabaul, Mexico</i>	10 Jul 2013	-3, 20	150, -95	16, 15	30, 15	O
<i>Pacaya</i>	15 Aug 2013	15	-91	16	43	O
<i>Sinabung, Ubinas</i>	15 Sep 2013	3, -16	98, -71	17, 15	35, 8	O
<i>Merapi, Nyamuragira, Pacaya</i>	18 Nov 2013	-7, -1, 15	110, 29, -91	17, 17, 15	30, 13, 8	O
<i>Sinabung, Nyamuragira</i>	9 Dec 2013	3, -1	98, 29	17, 16	26, 15	O

Table 2. Continued.

Volcano or region	Time	Latitude (°)	Longitude (°)	Altitude (km)	SO <sub>2</sub> (kt)	Instrument
Sinabung +	11 Jan 2014	3	98	16	29	O
Kelut	15 Feb 2014	−8	112	20	170	O
Merapi, Tungurahua	27 Mar 2014	−7, −1	110, −78	16, 16	31, 33	O
Santa Maria, Semeru	9 May 2014	15, −8	−91, 113	16, 16	25, 39	O
Sangeang-Api	31 May 2014	−8	119	17	60	O
Nyamuragira, Pavlof, Fuego, Dukono (Tungurahua)	9 Jul 2014	−1, 55, 14, 2	29, −162, −91, 128	16, 15, 15, 16	20, 10, 12, 20	O
Rabaul, Fuego	29 Aug 2014	−3, 14	150, −91	16, 16	36, 20	O
Nyamuragira	11 Sep 2014	−1	29	15	30	O
Ontakesan	27 Sep 2014	36	137	17	34	O
Sinabung, Turrialba	23 Oct 2014	3, 10	98, −84	17, 16	34, 17	O
Fogo, Semeru, Ubinas	24 Nov 2014	15, −8, −16	−24, 113, −71	17, 17, 16	11, 33, 11	O
Nevado del Ruiz, Nyamuragira, Vanuatu	16 Dec 2014	5, −1, −16	−76, 29, 168	15, 17, 16	8, 12, 21	O
Nyamuragira, Vanuatu, Honga Tonga	14 Jan 2015	−1, −16, −21	29, 168, −175	16, 16, 15	21, 17, 13	O
Vanuatu, Nyamuragira, Sopotan	16 Feb 2015	−16, −1, 1	168, 29, 124	17, 16, 16	13, 13, 13	O
Sopotan, Nevado del Ruiz, Santa Maria, Villarrica	8 Mar 2015	1, 5, 15, −39	125, −76, −91, −72	17, 16, 15, 15	14, 14, 8, 5	O
Tungurahua?, Batu Tara?	5 Apr 2015	−1, −8	−78, 124	17, 17	17, 22	O
Calbuco	25 Apr 2015	−41	−73	18	292	O
Manam, Tungurahua?	8 May 2015	−4, −1	144, −78	17, 17	24, 25	O
Wolf, Aira + Kuchinoerabujima	26 May 2015	0, 32, 30	−91, 131, 130	16, 15	63, 20	O
Raung	4 Jul 2015	−5	110	17	27	O
Cotopaxi, Raung, Suwanosjima, Manam	14 Aug 2015	0, −5, 30, −4	−80, 110, 130, 144	16, 16, 16, 20	24, 18, 10, 16	O
Nev. Ruiz + Reventador, Fuego, Sumatra	21 Sep 2015	5, 14, 3	−76, −91, 98	16, 17, 16	13, 8, 19	O
Sinabung, Fuego, Cotopaxi, Copahue	15 Oct 2015	3, 14, 0, −38	98, −91, −80, −71	16, 17, 15, 15	30, 15, 6, 13	O
Lascar, Sinabung, Nyamuragira, Fuego	30 Oct 2015	−23, 3, −1, 14	−70, 98, 29, −91	17, 17, 16, 16	13, 17, 12, 17	O
Vanuatu, Tungurahua, Telica, Rinjani	17 Nov 2015	−16, −1, 13, −5	168, −78, −87, 116	18, 17, 17, 16	18, 20, 10, 18	O
Vanuatu, Reventador, Tengger	5 Dec 2015	−16, 0, 2	168, −78, 120	17, 16, 16	16, 15, 12	O
Reventador, Sinabung	18 Dec 2015	0, 3	−78, 100	17, 16	16, 16	O
Sopotan +, Reventador, Fuego	8 Jan 2016	1, 0, 14	125, −78, −91	16, 17, 14	25, 19, 5	O
Semeru, Fuego	10 Feb 2016	−8, 14	113, −91	17, 16	34, 25	O
Vanuatu +, Tungurahua	27 Feb 2016	−16, −1	168, −78	16, 16	24, 16	O
Tungurahua, Sinabung +, Pavlof	15 Mar 2016	−1, 3, 55	−78, 98, −162	16, 17, 15	23, 26, 7	O
Reventador, Sinabung +, Fuego, Aira	13 Apr 2016	0, 3, 14, 32	−78, 98, −91, 131	17, 16, 15, 15	18, 30, 17, 6	O
Fuego, Nyamuragira + Ecuador, Langila, Sinabung	7 May 2016	14, −1, −5, 3	−91, 29, 150, 98	16, 17, 16, 17	16, 18, 16, 26	O
Bulusan, Sinabung, Semeru, Mexico	10 Jun 2016	13, 3, 8, 15	125, 98, 113, −100	17, 16, 17, 16	16, 14, 16, 10	O
Rinjani, Sinabung, Santa Maria	1 Aug 2016	−5, 3, 15	116, 98, −91	16, 16, 16	10, 30, 24	O
Sinabung + Vanuatu, Fuego	28 Aug 2016	−16, 14	168, −91	16, 16	42, 23	O
Ubinas, Sinabung	3 Oct 2016	−16, 3	−71, 98	15, 16	16, 26	O
Sabancaya, Sinabung + Bulusan	5 Nov 2016	−16, 3	−72, 98	16, 16	38, 46	O
Dukono, Vanuatu, Sabancaya	12 Dec 2016	2, −16, −16	128, 168, −72	17, 18, 15	30, 28, 28	O

Table 2. Continued.

Volcano or region	Time	Latitude (°)	Longitude (°)	Altitude (km)	SO <sub>2</sub> (kt)	Instrument
Sabancaya, Reventador, Sinabung + Vanuatu	10 Jan 2017	−16, 0, 3	−72, −78, 98	16, 17, 17	20, 30, 23	O
Sabancaya, Colima, Sinabung	4 Feb 2017	−16, 19, 3	−72, −104, 98	15, 16, 16	17, 15, 25	O
Sabancaya, Dukono, Fuego, Manam + Vanuatu, Bogoslof, Nevados de Chillán	5 Mar 2017	−16, 2, 14, −16, 53, −37	−72, 128, −91, 168, −170, −71	16, 17, 17, 17, 15, 15	10, 18, 8, 28, 4, 5	O
Sabancaya, Nevado del Ruiz, Sinabung, Vanuatu, Klyuchevskoy	10 Apr 2017	−16, 5, 3, −16, 56	−72, −75, 98, 168, 160	16, 16, 16, 16, 15	8, 15, 19, 17, 2	O
Sinabung, Manam, Fuego	5 May 2017	3, −4, 14	98, 145, −91	16, 17, 17	26, 10, 19	O
Sheveluch + Bogoslof	19 May 2017	57	161	15	20	O
Santa Maria, Sheveluch +, Manam	16 Jun 2017	15, 57, −4	−91, 161, 145	16, 16, 15	11, 33, 6	O
Fuego, Sinabung +, Sheveluch +	5 Jul 2017	14, 3, 57	−91, 98, 161	15, 16, 15	22, 21, 4	O
Sinabung, Cristobal + Fuego, Sheveluch + Bogoslof	8 Aug 2017	3, 13, 54	98, −87, −168	16, 17, 16 (26?)	31, 27, 5	O
Tinakula + Ambae	21 Oct 2017	−10, −15	166, 168	15, 15	60	O
Agung, Ambae, Sabancaya	27 Nov 2017	−8, −15, −5	116, 168, −80	15, 16, 15	22, 7, 12	O
Mayon, Vanuatu, Sabancaya	22 Jan 2018	13, −15, −5	124, 168, −80	15, 17, 16	7, 20, 16	O
Fuego, Vanuatu	1 Feb 2018	14, −15	−91, 168	16, 16	20, 17	O
Sinabung, Vanuatu	19 Feb 2018	3, −15	98, 168	16, 16	14, 21	O
Ambae, Vanuatu	26 Mar 2018	−15	168	16	60	O
Ambae	6 Apr 2018	−15	168	17	91	O
Sabancaya	15 May 2018	−16	−72	16	16	O, T
Fuego	3 Jun 2018	14	−91	16	15	O, T
Fernandina	17 Jun 2018	0	−92	15	8	T
Agung, Sabancaya	28 Jun 2018	−8, −16	115, −72	17, 16	33, 23	O, T
Sierra Negra	8 Jul 2018	−1	−92	15	25	T
Ambae	20 Jul 2018	−15	168	17	228	O, T
Manam, Sabancaya	25 Aug 2018	−3, −16	144, −72	17, 16	25, 12	O, T
Krakatau, Sabancaya	23 Sep 2018	−6, −16	105, −72	16, 16	5, 11	O
Manam, Sopotan, Reventador + Sangay	4 Oct 2018	−3, 1, 0	144, 125, −78	16, 16, 16	7, 4, 22	O
Nev.Ruiz, Sabancaya	24 Oct 2018	5, −16	−75, −72	16, 16	22, 11	O
Fuego, Sabancaya, Krakatau	6 Nov 2018	14, −16, −6	−91, −72, 105	16, 16, 15	10, 16, 19	O
Fuego, Sabancaya, Bagana	26 Nov 2018	14, −16, −6	−91, −72, 155	16, 16, 16	8, 9, 12	O
Sabancaya, Manam, Sopotan, Vanuatu	8 Dec 2018	−16, −3, 1, −16	−72, 144, 125, 168	16, 17, 16, 15	24, 8, 4, 6	O
Krakatau, Vanuatu, Sabancaya	23 Dec 2018	−6, −16, −16	105, 168, −72	16, 15, 16	7, 6, 20	O
Krakatau, Sabancaya, Manam	4 Jan 2019	−6, −16, −3	105, −72, 144	17, 17, 16	5, 20, 9	O
Manam, Sabancaya	24 Jan 2019	−3, −16	144, −72	17, 16	23, 14	O
Manam, Sabancaya	14 Feb 2019	−3, −16	144, −72	16, 16	12, 13	O
Manam, Sabancaya, Mexico, Chile	19 Mar 2019	−3, −16, 18, −24	144, −72, −98, −68	17, 16, 18, 15	9, 12, 6, 7	O
Sabancaya, Manam, Nev.Ruiz, Gamalama	20 Apr 2019	−16, −3, 5, 1	−72, 144, −75, 128	17, 16, 16, 16	31, 12, 15, 7	O, T
Sinabung, Manam, Sabancaya	25 May 2019	3, −3, −16	98, 144, −72	17, 16, 16	11, 20, 21	O, T
Raikoike	22 Jun 2019	48	153	17	196	O
Raikoike, Ulawun	29 Jun 2019	48, −5	153, 151	15, 19	221, 107	O, T
Ubinas, Raikoike, Manam	19 Jul 2019	−16, 48, −3	−71, 153, 144	15, 16, 17	72, 141, 15	O, T
Ulawun, Mexico	3 Aug 2019	−5, 20	151, −100	19, 17	111, 12	O
Ubinas	16 Aug 2019	−16	−71	16	27	O, T

## 5 Implementation of SO<sub>2</sub> emissions in the EMAC model

In the new approach in this study the SO<sub>2</sub> plumes are incorporated into the model simulations by adding the satellite-derived three-dimensional perturbations of SO<sub>2</sub> mixing ratios to the simulated SO<sub>2</sub> at the time of the eruptions. In order to get the correct altitude distribution and to reduce additional errors caused by the low temporal resolution of the satellite data and possible numerical problems due to huge gradients or values out of the range of used procedures in the model, we did not implement the volcanic SO<sub>2</sub> emissions as point sources. A comparison with point source injections in two case studies is provided in Appendix C3.

Effusive eruptions and quiescent degassing volcanoes from the time-dependent monthly three-dimensional climatology of Diehl et al. (2012) were added to the tropospheric SO<sub>2</sub> background emissions in the model simulations and truncated at an altitude of 200 hPa to avoid double-counting in the stratosphere and uppermost troposphere since the original climatology also contains contributions of explosive volcanoes listed in Table 2 (only 1990 to 2009) (Brühl et al., 2018). In some cases, especially in the tropics, some SO<sub>2</sub> from degassing is transported by convection to the lowermost stratosphere (see e.g. 1998 in Fig. 6).

The SO<sub>2</sub> emissions of our inventory are used in the EMAC model simulations, resulting in the time series shown in Fig. 6, with mixing ratios between background conditions of a minimum of 0.001 ppbv (parts per billion by volume – 10<sup>-9</sup>) in volcanically quiescent periods and highly active volcanic conditions with a maximum of 114 ppbv (as indicated at the top of the colour key, 5 d average) after the Pinatubo eruption. Figure 6 shows the modelled vertical distribution of stratospheric SO<sub>2</sub> in the Junge aerosol layer with the local maximum of SO<sub>2</sub> around 25 to 30 km altitude (Höpfner et al., 2013), and typical mixing ratios of SO<sub>2</sub> are about 0.03 ppbv.

The volcanic eruptions in 1990 are included in the model during the spin-up phase of the model simulations (not shown), with the emissions of the first entry in Table 2 set to the upper limit consistent with the Smithsonian reports SAGE and TOMS. The low number of volcanic eruptions in 1991 and the following years might be due to the low coverage of satellite data and “saturation” effects of the satellite instrument (see Sect. 2.4 about SAGE). The signatures of medium and small volcanic eruptions are too weak to be seen during the high concentrations in the first years after the Pinatubo eruption. There are also fewer entries in the Smithsonian database. From 2002 onwards, a higher number of small volcanic eruptions are captured in the volcanic sulfur emission inventory. This might be rather due to the improved data coverage enabled by a larger number of satellite instruments than to higher volcanic activity.

In most cases, the lower stratospheric SO<sub>2</sub> mixing ratios are highest at tropical latitudes. For this reason, tropical regions (20° S–20° N) are chosen for the vertical dis-

tribution in the lower illustration of Fig. 6 and the subsequent figures. Exceptions to this typical SO<sub>2</sub> pattern are single medium strong volcanic eruptions at high latitudes like Kasatochi (2008), Sarychev (2009) and Raikoke (2019) in the Northern Hemisphere or Calbuco (2015) in the Southern Hemisphere. Another noteworthy case is the Nabro (2011) eruption, where the volcanic emissions were transported from the tropics to northern latitudes by the Asian monsoon circulation (Bourassa et al., 2012b; Clarisse et al., 2014; Fairlie et al., 2014).

MIPAS typically captures background SO<sub>2</sub> mixing ratios in the lowermost tropical stratosphere at 16 to 17 km of around 0.02 to 0.05 ppbv (Fig. 1), which can be reproduced by our model by considering many more volcanoes than listed in the online National Aeronautics and Space Administration (NASA) SO<sub>2</sub> database (<https://so2.gsfc.nasa.gov>, last access: 10 January 2023) or most other databases in ISAMIP, e.g. Mills et al. (2016). Some time periods with low volcanic activity resulting in almost stratospheric background conditions can be identified between 1996 and 2004. To reach realistic SO<sub>2</sub> mixing ratios in the lower tropical stratosphere during these years, the contribution from oxidation of DMS and other sulfur species is important. Figure 6b shows increasing SO<sub>2</sub> with altitudes of above 23 km due to additional production from OCS photolysis.

The comparison of the simulated and observed SO<sub>2</sub> values shows that the volcanic SO<sub>2</sub> emissions from the volcanic sulfur emission inventory in Table 2 correlate well with the peaks of the mixing ratios in Fig. 6, as they dominate the stratospheric sulfur burden. In the stratosphere, SO<sub>2</sub> is converted to sulfate aerosol, which explains most of the inter-annual variability of the stratospheric aerosol burden as well as its influence on the stratospheric radiation. Generally, the conversion of SO<sub>2</sub> to sulfate aerosol particles depends on several factors, such as the altitude, latitude, or season of the eruption, and takes according to Höpfner et al. (2015) about 13, 23, and 32 d at 10–14, 14–18, and 18–22 km altitude, respectively, at mid latitudes. Carn et al. (2016) report an *e*-folding time varying between 2 and 40 d. The range agrees with our simulations (and assumptions in Sect. 4). Enhanced SO<sub>2</sub> concentrations from Pinatubo via photolysis of gaseous H<sub>2</sub>SO<sub>4</sub> remained in the mesosphere for several years (Brühl et al., 2015; Rinsland et al., 1995).

## 6 Climate impact of stratospheric aerosol in EMAC simulations

We compared the global influence of sulfur emissions on different atmospheric optical parameters. Based on Mie theory look-up tables, optical properties such as optical depth, single scattering albedo and asymmetry factor, which are used in radiative transfer simulations, were calculated online for different aerosol types: inorganics including sulfate, dust, organic carbon and black carbon, sea salt, and aerosol water

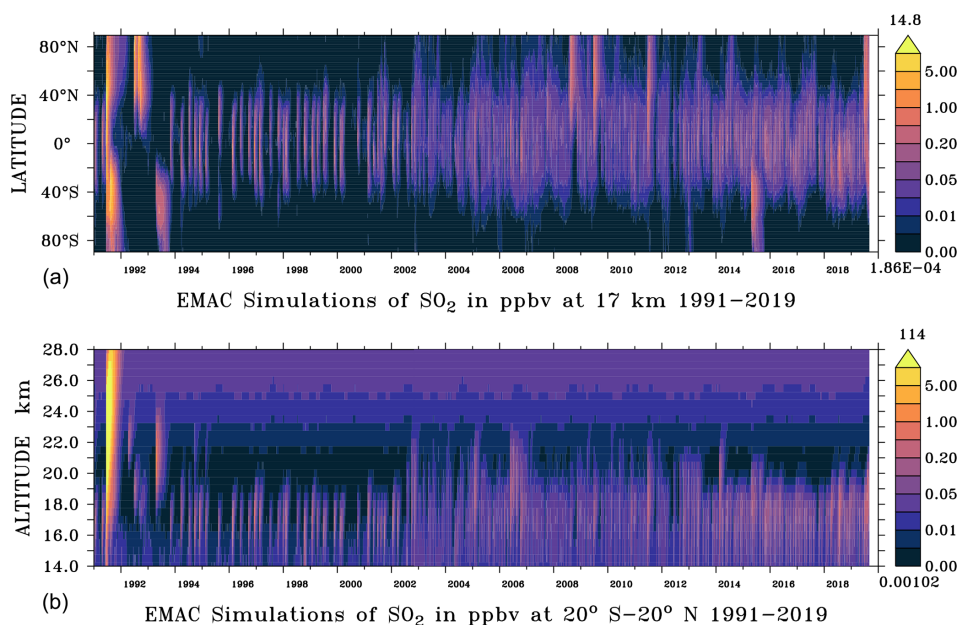


**Figure 6.** EMAC simulation of the stratospheric SO<sub>2</sub> mixing ratios (ppbv) (January 1991–August 2019, 5 d averages) using the volcanic sulfur emission inventory (Table 2) at 17 km altitude (a) and in vertical distribution for tropical regions 20° S–20° N (b). Maximum and minimum values are indicated above (yellow) and below (dark blue) the colour keys, respectively.

(Dietmüller et al., 2016). Via multiple calls of the radiation module RAD with and without (stratospheric) aerosol, the influence of stratospheric aerosol on instantaneous radiative forcing and heating is computed online (see Sect. 3). Also, the feedback to atmospheric dynamics is included.

### 6.1 EMAC simulations of the stratospheric aerosol extinction

Figures 7 and 8 show the global stratospheric aerosol extinction coefficients (in decadal logarithm) for the period 1991–2019 at 750 and 550 nm wavelengths of the EMAC model simulations at 17 km altitude and the vertical profile in tropical regions for 20° S–20° N. For medium eruptions, the maximum of the aerosol extinction lies at an altitude between 16 and 18 km. For this reason, an altitude of 17 km is chosen in the following analyses.

Figure 7 also shows the extinctions observed by OSIRIS and SAGE (interpolated from the observations at 525 and 1020 nm). The strongest event in these model simulations is the Pinatubo eruption in 1991 (see Table 2), which dominates the stratospheric aerosol extinction coefficient for more than 3 years after the eruption with a global distribution from the Equator to the poles in both hemispheres and a maximum altitude of more than 26 km. All other eruptions are significantly smaller, and for this reason a logarithmic scale is chosen. For further comparisons at 750 nm with GOMOS and OSIRIS, we refer to Figs. 3, 4, and Brühl et al. (2018).

The EMAC model simulations of the aerosol extinction coefficients at 550 nm (Fig. 8) agree well with the satel-

lite measurements of GOMOS (Fig. 2), SAGE II (Fig. 5), and GloSSAC (Appendix C) for the aerosol layer at an altitude of 16–22 km, where measured extinction values exceed  $\approx 2 \times 10^{-4} \text{ km}^{-1}$ . Above about 24 km EMAC is lower than the observations, likely because in the model meteoric dust particles were not considered.

Figures 7 and 8 show a similar distribution of the aerosol extinction at wavelengths of 550 and 750 nm. Due to the typical size and composition of stratospheric aerosol particles, the aerosol extinction is higher at 550 than at 750 nm. The peaks caused by mineral dust particles during summer in the northern sub-tropics are more pronounced at 750 than at 550 nm.

Despite the presence of volcanoes in the Antarctic (like Mount Erebus), the seasonal change in the extinction coefficient around 80° S is not due to volcanic eruptions but to the presence of polar stratospheric clouds (PSCs) as simulated by the model.

### 6.2 EMAC simulations of AOD

For practical reasons, the total stratospheric AOD is obtained by the vertical integral of the aerosol extinction above an altitude of about 16 km in the tropics and above about 13 km for mid latitudes and high latitudes, to allow for a direct comparison with the existing literature (Santer et al., 2014; Glantz et al., 2014) and satellite data. The stratospheric AOD is shown on a logarithmic scale in Figs. 9 and 10 with the new model simulations (red line) compared to satellite observations (light blue, grey, and blue lines). Using the wavelengths

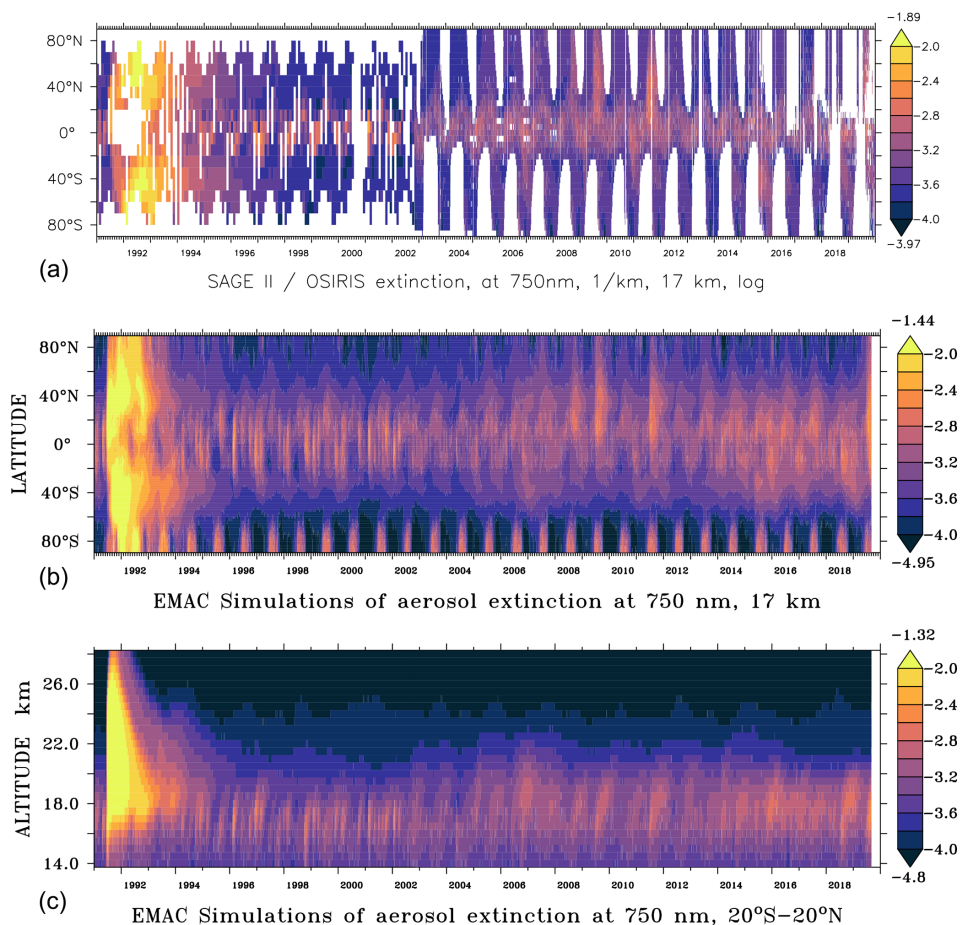


**Figure 7.** Comparison of stratospheric aerosol extinction for the 750 nm wavelength at 17 km altitude between the model simulations (b) and SAGE II and OSIRIS satellite data (a); all values on a logarithmic scale  $\log(\text{km}^{-1})$ . Vertical distribution of EMAC results for tropical regions  $20^{\circ}\text{S}$ – $20^{\circ}\text{N}$  in panel (c). Maximum and minimum values appear above (yellow) and below (dark blue) the colour keys, respectively. Five-day averages, except for monthly SAGE data.

of the satellites in the calculations (Sect. 3) avoids introducing additional errors through the use of conversion factors to adjust the values between the different wavelengths.

From 1991 to 2012, SAGE II (light blue line), GOMOS (grey line), and SAGE + CALIPSO and SAGE + OSIRIS (blue line) provide satellite data at a wavelength of 550 nm (OSIRIS data were converted from 750 nm by Glantz et al., 2014), shown in Fig. 9. For comparison, GloSSAC (Kovilakam et al., 2020) is also included as a black line in the upper panels using the vertical integral over extinction.

The maximum is reached after the Pinatubo eruption with a stratospheric AOD of 0.4 in the tropics (Fig. 9, upper panel, EMAC), being an order of magnitude larger than the following medium eruptions with a stratospheric AOD of about 0.01 (e.g. Manam in early 1997, Rabaul in 2006, and Nabro in 2011). The differences after the large Pinatubo eruption in 1991 between the model simulations and the SAGE II observations are related to the “saturation” effects of the satellite instrument (i.e. data gaps due to an opaque path through

the atmosphere at the tangent point) and can be observed for more than 1 year, also shown above in Fig. 5. In GloSSAC, gap filling (with lidar and CLAES data) was applied for this case. In this study about 17 Tg  $\text{SO}_2$  was injected for the Pinatubo eruption (Guo et al., 2004). Model comparisons by Timmreck et al. (2018) show that the span of the used injections varies between 10 Tg  $\text{SO}_2$  (e.g. Dhomse et al., 2014; Mills et al., 2016; Schmidt et al., 2018) and 20 Tg  $\text{SO}_2$  (e.g. English et al., 2013). Thus, this study is within the range of the injected sulfur masses. On the other hand, filling the gaps in the SAGE data just by horizontal linear interpolation increases the peak AOD by about a factor of 2, which is close to the GloSSAC compilation. In Fig. 10 the AOD from the AVHRR (Advanced Very High Resolution Radiometer) by Long and Stowe (1994) at 630 nm is included, which is close to our simulations. Consistent with the typical wavelength dependence, these values lie between the red curves for 550 nm (Fig. 9) and 750 nm (Fig. 10) at the peak after the Pinatubo eruption.

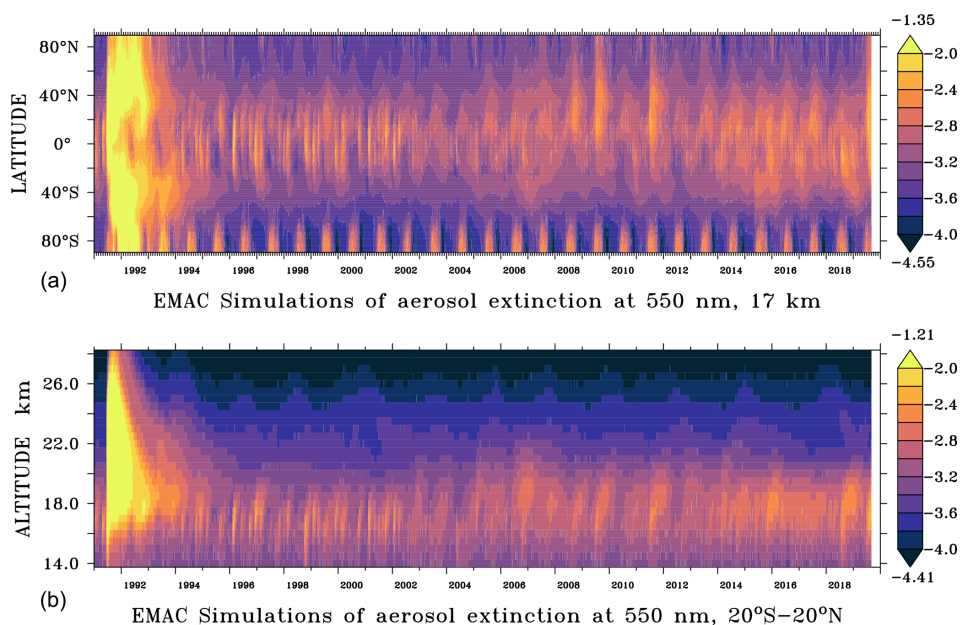


**Figure 8.** EMAC simulation of the stratospheric aerosol extinction on a logarithmic scale  $\log(\text{km}^{-1})$  for a 550 nm wavelength from January 1991 to August 2019 (5 d averages), zonal mean at 17 km altitude (a) and vertical distribution for tropical regions 20° S–20° N (b). Maximum and minimum values appear above (yellow) and below (dark blue) the colour keys, respectively.

When comparing the EMAC simulations (red line in Fig. 9) with the simulation of Schmidt et al. (2018) (black line in Fig. 9c), it can be recognized that a smaller value for the peak of the Pinatubo eruption occurs. Here it needs to be considered that Schmidt et al. (2018) inject less  $\text{SO}_2$ . For Pinatubo, monthly averaging reduces the peak in EMAC by about 5 %, and the smaller events cause fluctuations of up to  $\pm 0.007$  (see Supplement Fig. S2).

Between 1993 and 1996 the reduction in the stratospheric AOD in the model simulations is faster than indicated by the satellite observations and in Schmidt et al. (2018). This indicates that the removal of stratospheric aerosol is still too rapid when applying our modal model. Schmidt et al. (2018) show a slower decrease in AOD after the Pinatubo eruption. This could indicate that EMAC still needs better fine-tuning of the size distribution modes or addition of modes in the aerosol sub-model to improve the aerosol removal in the stratosphere. Additionally, smaller volcanic eruptions might be missing in view of the low number of identified events in the years after the Pinatubo eruption.

In Fig. 10, the coverage of GOMOS (grey line) is often too low at a wavelength of 750 nm for the years from 2002 to 2012, so the inclusion of OSIRIS data (blue line) is important (Brühl et al., 2018). For the years after 2012 the timeline only contains data from OSIRIS at the 750 nm wavelength.

Nevertheless, there remain small differences between the model simulation and the observations, for instance in 2010, which indicates missing volcanic eruptions (or an underestimation of the Merapi eruption by MIPAS compared to OSIRIS, Appendix B, or to other data, Mills et al., 2016).

The different distributions of the peaks in the upper and lower panels are related to the latitude of the volcanic eruptions. Emissions reaching the stratosphere from strong eruptions in the tropics are distributed by the Brewer–Dobson circulation over the Northern Hemisphere and Southern Hemisphere even to high latitudes, as in the cases of Soufriere Hills and Rabaul in 2006. However, if an eruption takes place at high latitudes (such as for Redoubt 2009) or at mid latitudes like Kasatochi (2008), Sarychev (2009) or Raikoke (2019), most of the emissions stay in the Northern Hemisphere, and the signal in the tropics is weaker. Our Northern Hemisphere results for AOD (at 550 nm) of about 0.025 after the Raikoke eruption agree within uncertainties with Kloss et al. (2021), who use different satellites and different modelling approaches.

### 6.3 EMAC simulations comparing the radiative forcing at the top of the atmosphere

The instantaneous radiative forcing of the stratospheric aerosol is calculated by multiple calls of the RAD sub-model (Sect. 3). The simulated global instantaneous radiative forcing in  $\text{W m}^{-2}$  of stratospheric aerosol at the top of the atmosphere (TOA) is illustrated in Fig. 11.

As the Pinatubo eruption caused a negative radiative forcing of more than an order of magnitude greater than all other eruptions since then, the figure is sub-divided into two panels with different scalings. The lower panel shows the relatively small values. The new model simulations for the instantaneous radiative forcing at the TOA with the additional vol-

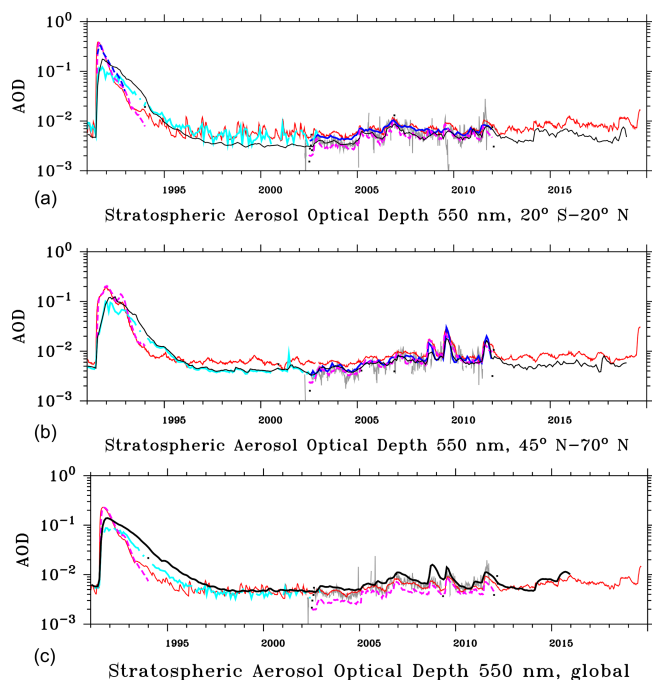


**Figure 9.** Stratospheric AOD at 550 nm wavelength: tropical regions 20° S–20° N above 16 km are shown in panel (a), the Northern Hemisphere 45–70° N above about 13 km in panel (b) and global means in panel (c). Satellite observations from SAGE II (Thomason et al., 2008) are indicated by the light blue line, GOMOS (Bingen et al., 2017) by the grey line and values derived from SAGE + CALIPSO (a) (Santer et al., 2014) and SAGE + OSIRIS (b) (Glantz et al., 2014) by the blue line. The red line shows the EMAC model simulations using the three-dimensional SO<sub>2</sub> injections of Table 2 compared to the simulations of Brühl et al. (2015) (pink dashed line) and the global stratospheric AOD from Schmidt et al. (2018) (black line in panel c). The black line in panels (a) and (b) represents GloSSAC, derived from extinction at 525 nm. For the Pinatubo period the dashed blue line shows the AVHRR observations by Long and Stowe (1994) at 630 nm (a). EMAC and GOMOS as 5 d averages, other data monthly.

canic eruptions (red line) are closer to the estimates from satellite extinction measurements of SAGE, GOMOS, and CALIOP by Solomon et al. (2011) (grey bars) than in previous studies (e.g. Brühl et al., 2015, pink dashed line, and Brühl et al., 2018, blue dashed line). For the TOA, see Supplement Fig. S1). In Fig. 11 the published forcing values at the tropical tropopause of the previous studies are shown, which are systematically more negative than the values at the TOA. For Sarychev it is clear that this cannot compensate for the effect of the neglect of aerosol in the extratropical lowermost stratosphere. A comparison with volcanic effective radiative forcing (aerosol–radiation interactions) from Schmidt et al. (2018) is shown by the black line, including a forcing of  $-0.05 \text{ W m}^{-2}$  for the stratospheric background aerosol (derived from the numbers provided). Especially for high-latitude eruptions their effective forcing (ari

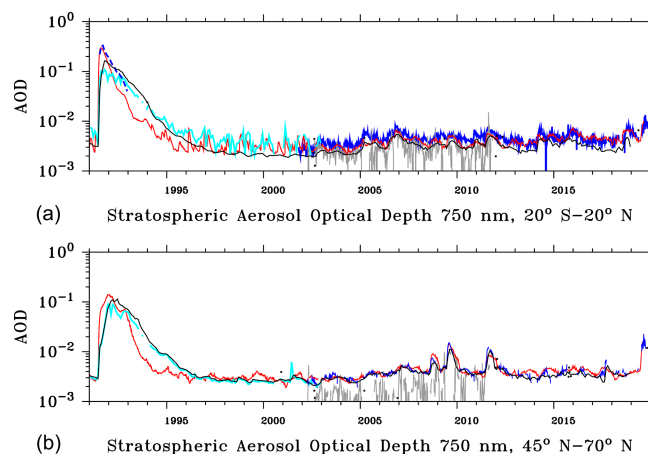


**Figure 10.** Stratospheric AOD at 750 nm wavelength: tropical regions 20° S–20° N above 16 km are shown in (a) and for the Northern Hemisphere 45–70° N above 13 km in (b). Satellite observations from OSIRIS (Rieger et al., 2019) are indicated by the blue line and GOMOS (Bingen et al., 2017) by the grey line. For the Pinatubo period the dashed blue line shows the AVHRR observations by Long and Stowe (1994) at 630 nm (a). The light blue line shows the interpolation of SAGE data at the 525 nm and 1020 nm wavelengths. The EMAC model simulations, using the three-dimensional SO<sub>2</sub> injections of Table 2, are shown by the red line. The black line represents GloSSAC, derived from extinction at 525 and 1020 nm. EMAC, GOMOS, and OSIRIS as 5 d averages, other data monthly.

is larger than instantaneous forcing in EMAC and the annual averages of Solomon et al. (2011), also because of a higher aerosol load in the lowermost stratosphere than in EMAC (see sensitivity studies for Sarychev in Appendix C3). In the period considered here, the volcanoes are the dominant factor in (instantaneous) global radiative forcing. Background stratospheric aerosol like sulfate from other sources, dust, and organics contributes about  $-0.04 \text{ W m}^{-2}$  to the value of the order of  $-0.1 \text{ W m}^{-2}$  at the TOA in volcanically quiescent periods (e.g. in 2000, 2002, or 2004). At the TOA absolute values up to  $-0.2 \text{ W m}^{-2}$  ( $-0.14 \text{ W m}^{-2}$  old approach where only aerosol above 100 hPa was considered) are reached following Rabaul (2006), Kasatochi (2008), Nabro (2011), and Calbuco/Sinabung (2015) and are stronger than  $-0.32 \text{ W m}^{-2}$  (old approach  $-0.2 \text{ W m}^{-2}$ ) following the Raikoke/Ulawun (2019) eruptions. The value for Raikoke/Ulawun is within the range discussed in Kloss et al. (2021).

The strongest instantaneous global radiative forcing in the model simulations is caused by the Pinatubo eruption with a maximum of about  $-5 \text{ W m}^{-2}$  at the TOA for the solar part ( $-4 \text{ W m}^{-2}$  for solar + IR forcing at the TOA); this is in good agreement with the results of Minnis et al. (1993) and the observations of the ERBE satellite (light blue crosses in Fig. 11). Schmidt et al. (2018) estimate the effective forcing from the difference of a simulation with and without volcanoes injecting into the stratosphere, i.e. including dynamical

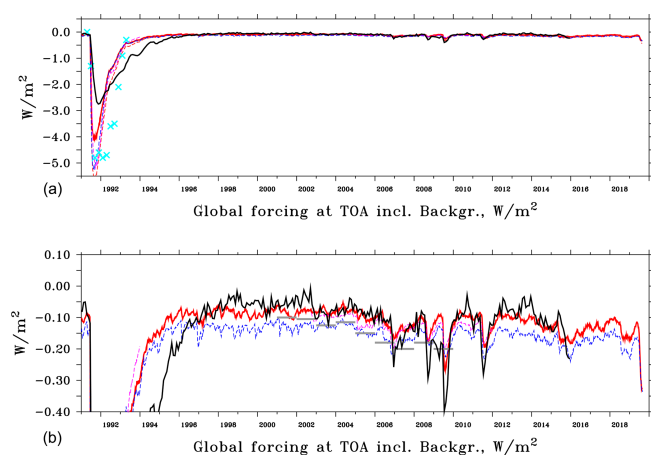


**Figure 11.** EMAC instantaneous radiative forcing by stratospheric aerosol (red, pink, and blue lines, 5 d averages). Solar forcing at the top of the atmosphere (TOA) (dashed red line, **a**) is compared to solar forcing at the TOA from satellite observations of the Earth Radiation Budget Experiment (ERBE), 72 d means, and light blue crosses (Wong et al., 2006; Toohy et al., 2011). The full red line displays the total (solar + IR) forcing at the TOA, including contributions from aerosol down to the calculated tropopause. The blue dashed line shows the total forcing using the previous scheme at the tropical tropopause (Brühl et al., 2018), the dashed pink line the same with fewer volcanoes of Brühl et al. (2015). Grey bars show annual averages derived from observations by Solomon et al. (2011). The black line shows results from Schmidt et al. (2018) with volcanic effective radiative forcing (aerosol–radiation interactions) at the TOA, including a background aerosol forcing of  $-0.05 \text{ W m}^{-2}$ . Panel (**b**) is an enhanced representation of panel (**a**).

and chemical adjustments (effect for Pinatubo up to about  $0.4 \text{ W m}^{-2}$ ). For Pinatubo monthly averaging instead of 5 d averaging reduces the peak by  $0.2 \text{ W m}^{-2}$ , and the smaller events cause fluctuations of up to  $\pm 0.02 \text{ W m}^{-2}$  (i.e. 50 % of the background; see Supplement Fig. S3) at the fine temporal resolution.

#### 6.4 EMAC simulations of the stratospheric aerosol radiative heating

The simulated instantaneous aerosol radiative heating in the model is derived from multiple radiation calls with and without aerosol in the RAD radiation sub-model. Figure 12 shows the calculated local heating effects in the stratospheric aerosol layer. Small and medium volcanic eruptions have the largest effects between altitudes of 17 and 18 km and generate an atmospheric heating of up to  $0.03 \text{ K d}^{-1}$ . The eruption of Pinatubo, on the other hand, had significantly stronger effects at altitudes of 20 to 25 km and caused atmospheric heating of more than  $0.7 \text{ K d}^{-1}$ , which corresponds quite well to the results of Rieger et al. (2020) showing a maximum of the instantaneous solar heating rate of  $0.5 \text{ K d}^{-1}$  in the tropics near 24 km plus instantaneous thermal heating rates of about

$0.2\text{--}0.3 \text{ K d}^{-1}$ . This is about 23 times greater than all other eruptions in the model simulation, including the Raikoke eruption in 2019.

Further, a seasonal signal contributes significantly to the radiative heating in the northern sub-tropics. This is caused by transport of desert dust to the UTLS, mostly via the Asian summer monsoon convection, which generates additional heating during the time of the Asian summer monsoon (Brühl et al., 2018).

## 7 Discussion and conclusions

The objective of this study was to generate a detailed volcanic sulfur emission inventory and to improve the EMAC model simulations of the global stratospheric aerosol and sulfate burden and compute the long-term volcano-induced instantaneous radiative forcing using computed extinctions validated on the basis of satellite data.

The presented approach, based on observed three-dimensional perturbations of  $\text{SO}_2$  or extinction due to volcanic eruptions, avoids uncertainties related to the point source approach due to required additional assumptions and possible numerical artifacts related to the extreme perturbations by several orders of magnitude in small regions and non-linear feedback processes. Our case studies on this show large uncertainty in computed instantaneous radiative forcing and the possible development of spurious long-lived mesoscale vortices containing very high sulfate. In our approach the largest uncertainties are due to the handling of gaps in the satellite data.

Updated OSIRIS data allowed us to extend the comparisons of Brühl et al. (2018) to the year 2019; a detailed analysis of Level-2 SAGE II data (individual profiles of extinction at two wavelengths and SAD) together with the Smithsonian volcano database was used to extend the comparison back to 1990. As a result, the simulations in this paper encompass a total of 29 years and cover the period 1991 to 2019 compared with 2002 to 2012 in our previous work. The temporal resolution is 5 d for the three instruments MIPAS, GOMOS, and OSIRIS, and it is possible to identify multiple volcanic eruptions within a short period of time. With the three-dimensional datasets, the vertical distribution of  $\text{SO}_2$  can be distinguished and the amount of sulfur reaching the stratosphere can be calculated much more accurately than by estimation from a total column. Tropospheric sulfur emissions are treated separately.

Our volcanic sulfur emission inventory is an extension and improvement of the versions published by Bingen et al. (2017) and Brühl et al. (2018). While the previous version included 230 explosive volcanic eruptions, the new version includes more than 500 eruptions. An overview of these eruptions is given in the volcanic sulfur emission inventory in Table 2, which indicates the estimated stratospheric  $\text{SO}_2$  emissions as well as the plume altitudes. These consist of about

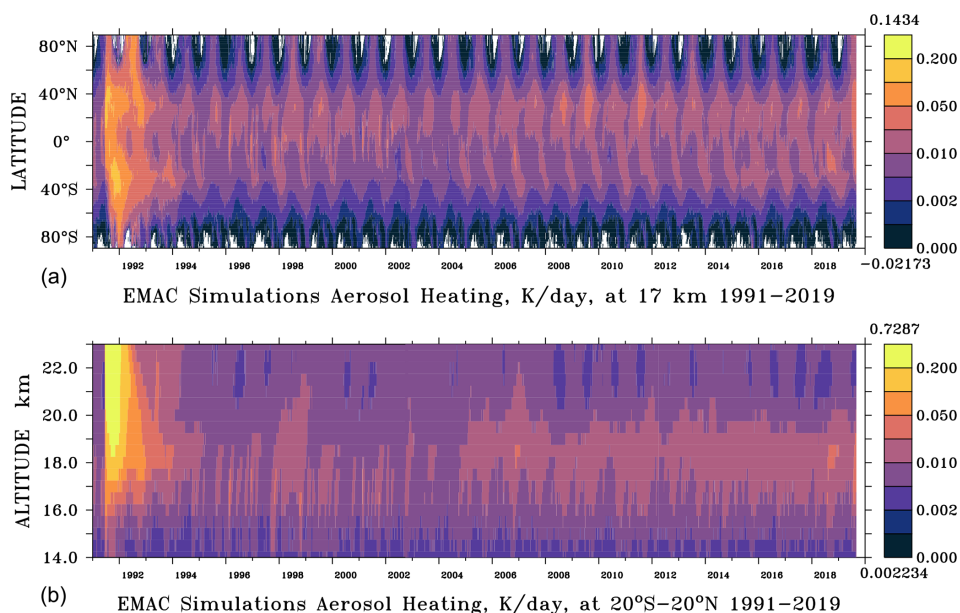


**Figure 12.** EMAC simulation of the aerosol radiative heating in  $\text{K d}^{-1}$  for solar and infrared radiation from January 1991 to August 2019 (5 d averages) based on the volcanic sulfur emission inventory (Table 2), in horizontal distribution at 17 km altitude (a) and in vertical distribution for tropical regions  $20^{\circ}\text{S}$ – $20^{\circ}\text{N}$  (b).

80 eruptions in the first time period between 1990 and 2002 measured by the SAGE II instrument, 240 eruptions in 2002–2012 measured with multiple instruments, and 230 eruptions in the last time period 2012–2019 measured by OSIRIS. The consequence of the inclusion of many more small-sized eruptions reaching the UTLS is that stratospheric aerosol optical depth and radiative forcing do not decrease to the non-volcanic background between medium-sized eruptions, in agreement with observations.

Strong volcanic eruptions can inject several teragrams of  $\text{SO}_2$  directly into the stratosphere. For this reason, the maxima of the global stratospheric  $\text{SO}_2$  concentrations correlate well with the eruption events of the volcanic sulfur emission inventory in Table 2. The  $\text{SO}_2$  emissions of smaller volcanic eruptions can reach the lower stratosphere by convective transport through the tropical tropopause, which results in accumulation of sulfate aerosol in the lower stratosphere. This was demonstrated to be important for correctly modelling the AOD in volcanically quiescent periods.

Our analysis shows the importance of using multi-instrument satellite datasets to fill data gaps and to detect as many volcanic eruptions as possible. The optimal data coverage time period is from 2002 to 2012, for which simultaneous measurements from the MIPAS, GOMOS, and OSIRIS instruments are available. For 2002 to 2005 this also includes SAGE II. The periods with simultaneous observations by MIPAS and the other instruments were used to develop and validate a method for estimating injected  $\text{SO}_2$  and its distribution from extinction observations. The evaluation by the satellite datasets shows that GOMOS is important for detecting

volcanic eruptions during MIPAS data gaps and for a better attribution of individual eruptions. Consequently, the combination of MIPAS, GOMOS, and OSIRIS data leads to an improved  $\text{SO}_2$  emission database for calculating the instantaneous radiative forcing in the EMAC chemistry-climate model.

Large volcanic ash plumes can interfere with the  $\text{SO}_2$  signal in satellite measurements, and satellites could be “blind” during the first few days or months after an eruption (Höpfner et al., 2015). However, most volcanic ash particles are relatively large and sediment after some hours or days, and hence they only have minor climatic significance (Boucher, 2015) and are not discussed in detail here. There are, however, volcanoes (e.g. the eruption of Kelut in 2014; Zhu et al., 2020) which emitted small ash particles which can stay in the lower stratosphere for several months (Vernier et al., 2016). Moreover, we found that the model set-up might have to be improved by including an additional aerosol mode to reduce the removal by sedimentation of stratospheric aerosol after large volcanic eruptions. Some satellite datasets are affected by gaps and noise. Comparing the model results with OSIRIS data in the tropics (Fig. 10) indicates that some volcanic events are underestimated or missing in the volcanic sulfur emission inventory in the year 2010.

Frequent volcanic eruptions of moderate and small intensities, injecting sulfur gases into the upper troposphere and lower stratosphere, contribute significantly to the stratospheric aerosol layer, in particular through their accumulation in time. These cause a global negative instantaneous radiative forcing of the order of more than  $0.1\text{ W m}^{-2}$

at the TOA, including a background aerosol forcing of about  $0.04 \text{ W m}^{-2}$ . For example, after the eruptions of Soufriere Hills/Rabaul (2006) and Nabro (2011) and the combination of the Sinabung, Wolf, and Calbuco eruptions (2015), a negative instantaneous radiative forcing of  $0.2 \text{ W m}^{-2}$  ( $0.14 \text{ W m}^{-2}$ , old approach) and  $0.32 \text{ W m}^{-2}$  ( $0.2 \text{ W m}^{-2}$ , old approach) was reached after Raikoke/Ulawun (2019) at the TOA.

Note that for the calculation of the instantaneous forcing by these medium-sized eruptions, it is essential to consider the radiative effect of volcanic aerosol down to the tropopause (Ridley et al., 2014). Including only the aerosol above the 100 hPa level as done in Brühl et al. (2018, 2015) can lead to significant underestimates which were partially hidden in these studies by showing the instantaneous forcing at the tropopause which is about  $0.08 \text{ W m}^{-2}$  stronger than at the TOA in EMAC.

The model also includes mineral dust and organics transported from the lower troposphere to the UTLS. The EMAC simulations show a seasonal signal in the stratospheric AOD and an enhanced radiative heating in the Northern Hemisphere induced by the convective transport of mineral dust to the UTLS in the Asian monsoon region. This is confirmed by satellite observations and by Klingmüller et al. (2018). The influence of wildfires and other biomass burning plumes on stratospheric AOD has increased in recent years (Fromm et al., 2019), and this effect should be included in the model to account for perturbations in organic and black carbon.

#### Appendix A: List of Modular Earth Submodel System (MESSy) sub-models used in this study

The computations for this study were performed on the Mistral supercomputer at the Deutsches Klimarechenzentrum (DKRZ), Hamburg, Germany. For this purpose, EMAC (ECHAM5/MESSy Atmospheric Chemistry), a coupled atmospheric circulation model consisting of the 5th generation of the European Centre Hamburg general circulation model (ECHAM5) and the MESSy (V2.52), was used.

ECHAM5 (5th generation of the European Centre Hamburg general circulation model) is an atmospheric general circulation model (Roeckner et al., 2003, 2006), which runs with the self-consistent quasi-biennial oscillation (QBO). It is nudged to the meteorological ERA-Interim reanalysis data of the European Centre for Medium-Range Weather Forecasts (ECMWF) up to about 100 hPa. To avoid a phase drift, we used the QBO sub-model for weak nudging to the QBO zonal wind observations (Giorgetta et al., 2002).

MESSy is an Earth system model, which consists of several sub-models (Jöckel et al., 2005, 2006, 2010). An overview of the sub-models used in this study is given in Table A1.

Mineral dust emissions are calculated online using the emission scheme of Astitha et al. (2012) as part of the ONE-MIS sub-model. The sub-model TREXP (Jöckel et al., 2010) is needed to inject  $\text{SO}_2$  emissions in point source emission simulations. The convection was calculated with the CONVECT sub-model (Tost et al., 2006b), with the convection scheme from Tiedtke (1989) and the Nordeng (1994) closure. The convection parametrization is sensitive to the model resolution, which results in differences between different model resolutions in the vertical transport of tracers, like dust, water vapour, ozone, and  $\text{SO}_2$ , especially near the low-latitude tropopause (Brühl et al., 2018).

The loss of gas-phase species to the aerosol is parameterized in the third EQUilibrium Simplified Aerosol Model (EQSAM3) (Metzger and Lelieveld, 2007). The uptake of gases on wet particles and on acid aerosol particles is included in the model calculation. Concerning removal mechanisms, the SCAVENGING sub-model calculates the loss of atmospheric tracers and aerosols by wet deposition as well as the liquid-phase chemistry in clouds and precipitation (Tost et al., 2006a). The chemistry of the CAABA/MECCA sub-model contains photolysis reactions, which need photolysis rate coefficients ( $J$  values) for tropospheric and stratospheric species computed by the JVAL sub-model. The RAD\_FUBRAD sub-sub-model is used to calculate the short-wave heating rates from the absorption of UV by  $\text{O}_2$  and  $\text{O}_3$  in the upper stratosphere and mesosphere. The lowest level of the RAD\_FUBRAD sub-sub-model for the upper atmosphere is shifted from above 70 hPa in the original version of Dietmüller et al. (2016) to 30–14 hPa to allow for scattering by the aerosol in the simulations with volcanic emissions.

**Table A1.** List of MESSy sub-models used. References and short description from <https://messy-interface.org/messy/submodels/> (last access: 10 January 2023). Parts of the base model copied into MESSy which must always be active are not listed here.

Sub-model	Function	Reference
AEROPT	Aerosol optical depth	Dietmüller et al. (2016)
AIRSEA	Air–sea exchange of trace gases	Pozzer et al. (2006)
CAABA/MECCA	Atmospheric chemistry	Sander et al. (2011)
CONVECT	Convection processes	Tost et al. (2006b)
CVTRANS	Convection transport of tracers	Tost et al. (2010)
DDEP	Dry deposition	Kerkweg et al. (2006a)
GMXe	Global Modal Aerosol eXtension	Pringle et al. (2010)
IMPORT	Import of external data files	Jöckel et al. (2006)
JVAL	Photolysis rate coefficients	Jöckel et al. (2006)
LNOX	NO <sub>x</sub> lightning production	Tost et al. (2007)
MSBM	Multiphase Stratospheric Box Model	Jöckel et al. (2010)
OFFEMIS	Offline emissions	Kerkweg et al. (2006b)
ONEMIS	Online emissions	Kerkweg et al. (2006b)
QBO	QBO nudging	Giorgetta et al. (2002)
RAD	Radiation	Dietmüller et al. (2016)
SCAV	Scavenging (wet removal)	Tost et al. (2006a)
SEDI	Aerosol sedimentation	Kerkweg et al. (2006a)
TNUDGE	Tracer nudging	Kerkweg et al. (2006b)
TREXP	Tracer release experiments from point sources	Jöckel et al. (2010)
TROPOP	Tropopause calculation	Jöckel et al. (2006)

## Appendix B: Comparison of volcanic injections derived from simultaneous MIPAS, SAGE, GOMOS and OSIRIS observations

The eruption of Reventador in the tropics in November 2002 has been shown to be an ideal case where simultaneous observations of all satellite sensors were available, so that the direct SO<sub>2</sub> observation could be used for development and validation of a conversion formula for the 750 nm extinction seen by GOMOS and OSIRIS, which also works approximately for SAGE if its observations at 525 and 1020 nm are interpolated to 750 nm. Here we first use the ratio between the model-calculated sulfate volume mixing ratio and its share in extinction at low latitudes of the lower stratosphere, which is typically  $1.2 \times 10^{12}$  per air density (molec. cm<sup>-3</sup>) for the period during which MIPAS was available. This works for medium- and small-sized eruptions and data available over about 4 weeks following the eruptions and if no other events occur less than about 4 weeks before, which is the case for the Reventador eruption. If the time lag of data is several weeks, a correction factor of  $> 1$  has to be applied in Eq. (1) to account for removal processes, and if another event is relatively close in time, the factor has to be  $< 1$  to remove the influence of the previous event (see Tables S1 and S2 in the Supplement, which also indicate additional uncertainties for a few cases in 2018 and 2019 due to too sparse data).

For Reventador the factor is 1 for all instruments (for OSIRIS 0.8 is slightly better because of remnants from the Ruang eruption about 4 weeks before). For all instruments the derived injected SO<sub>2</sub> mass is very close to 77 kt as shown in Table 2. The spatial patterns are similar, except that the zonal wind causes a shift in longitude due to the time lag from conversion of SO<sub>2</sub> to aerosol; see Fig. B1. In the case of SAGE, the alternative method of Grainger et al. (1995) involving aerosol surface area density (SAD) and aerosol volume density is more suitable for removing cloud perturbation and is used in the simulation. It is assumed that sulfate mixing ratios correspond to the SO<sub>2</sub> injected. Some uncertainty remains from removing the background, which we have done by subtracting a fraction of the derived SO<sub>2</sub> at the longitude where it has a minimum, i.e. the longitude where the effect of the volcano is smallest for all altitudes. If the extinctions at 525 and 1020 nm are used directly, the patterns are similar except for the lowermost part which contains more data gaps. This has also been checked for every event prior to MIPAS. Integrated injected SO<sub>2</sub> masses for all examples are provided in Table B1.

For the eruption of Merapi in November 2010 the satellite instruments do not agree. From OSIRIS about 70 % more injected SO<sub>2</sub> is derived than from MIPAS, i.e. 170 kt instead of 97 kt used in the transient simulation (see Table 2 and differences in Fig. 10). GOMOS has too sparse data here to obtain a proper integral directly, but patterns are similar (Fig. B2). If other information is available, the gaps can be filled with likely values in the region where the plume was

seen, a method which had to also be applied to some events seen by OSIRIS in 2018 and 2019 for which the data were sparse.

For high-latitude eruptions the longer conversion time of  $\text{SO}_2$  to sulfate compared to the tropics has to be considered, which, together with aerosol removal processes, leads to a weaker extinction signal. To account for this a correction factor of about 2 in the conversion formula for OSIRIS, for example for Sarychev in June 2009, leads to values consistent with the ones derived by MIPAS (Fig. B3). For the low-latitude eruption of Manda Hararo in the same entry of Table 2 (separated at  $24^\circ\text{N}$  for the integration), the factor of 1 is still appropriate.

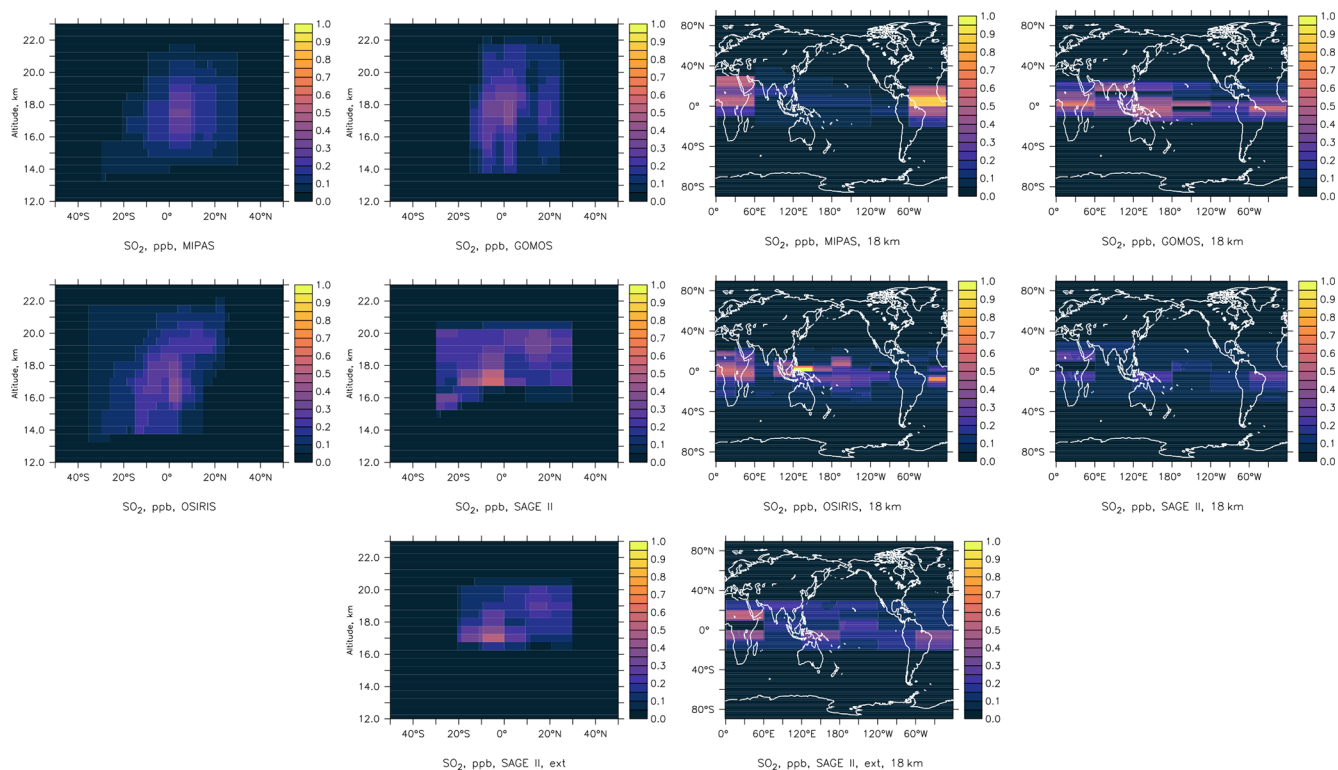


**Figure B1.** 2002 Reventador eruption:  $\text{SO}_2$  mixing ratio perturbation (ppb) derived from MIPAS and the three extinction instruments. MIPAS data of 7 to 17 November 2002, OSIRIS and GOMOS data of 11 to 22 November, and SAGE II orbits of November and early December 2002. Zonal average vertical distribution (left) and plumes at 18 km altitude (right). OSIRIS with a correction factor of 0.8 due to remnants from the Ruag eruption and SAGE II with the Grainger-based method. Lower row: SAGE II  $\text{SO}_2$  derived from extinction (interpolated to 750 nm from 525 and 1020 nm). Factor 1 is the default.

**Table B1.** Integrated mass of injected  $\text{SO}_2$  (kt) for the different methods in Figs. B1 to B3.

Eruption	MIPAS	GOMOS	filled	OSIRIS	SAGE II Gr.	ext.
Reventador 2002	77	75	–	89	80	50
Merapi 2010	97	18	77	170	–	–
Sarychev 2009	446	141	–	353	–	–
Manda Hararo 2009	82	81	–	101	–	–

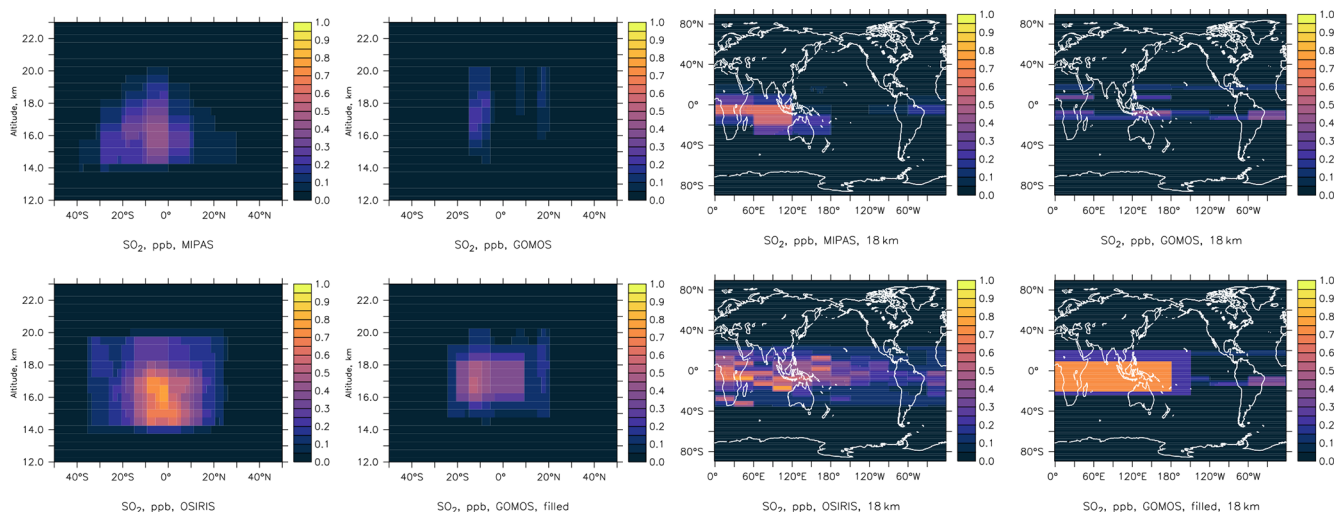


**Figure B2.** 2010 Merapi eruption:  $\text{SO}_2$  mixing ratio perturbation (ppb) derived from MIPAS, GOMOS OSIRIS and GOMOS with gap filling. MIPAS data 5 to 20 November 2010, OSIRIS 14 to 25 November, and GOMOS 25 November to 9 December (sparse data). Zonal average vertical distribution (left) and plumes at 18 km altitude (right).

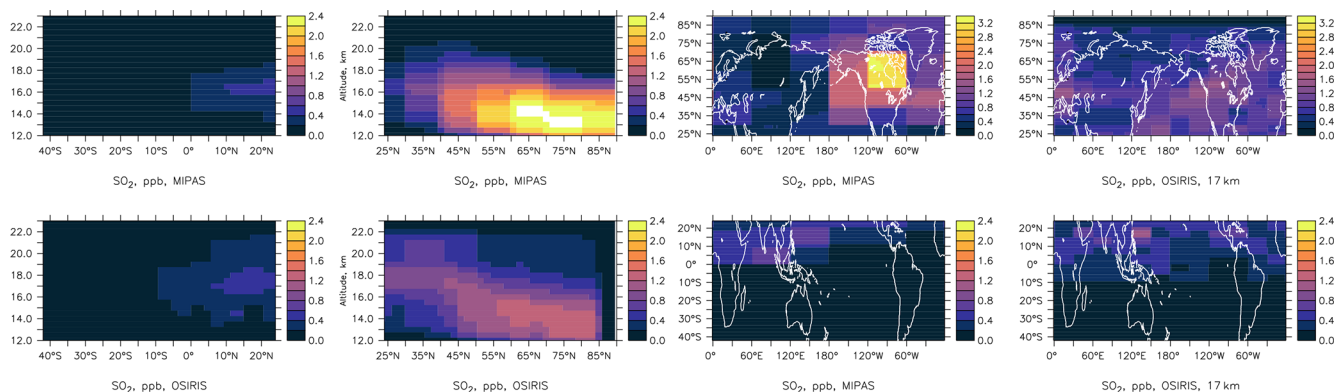


**Figure B3.** 2009 Sarychev (second column, upper right row) and Manda Hararo (first column, lower right row) eruptions:  $\text{SO}_2$  mixing ratio perturbation (ppb) derived from MIPAS and OSIRIS; arrangement of the panels because the event is split at  $24^\circ\text{N}$  as for integrated values in Table 2. MIPAS data 18 June to 18 July 2009, OSIRIS data 17 July to 3 August. Zonal average vertical distribution (left) and plumes at 17 km altitude (right).

## Appendix C: Comparison

### C1 Comparison with GloSSAC

Figure C1 shows the aerosol extinction of GloSSAC on the same logarithmic scale  $\log(\text{km}^{-1})$  as the used satellite datasets and the EMAC simulations in Figs. 2–8.

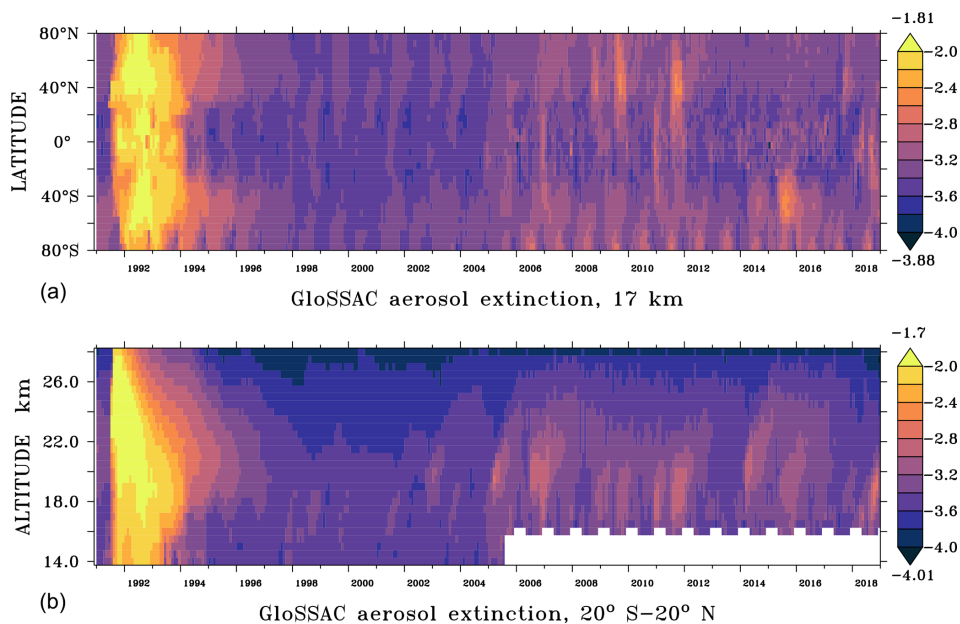


**Figure C1.** GloSSAC aerosol extinction on a logarithmic scale  $\log(\text{km}^{-1})$  for the 525 nm wavelength from the January 1991–December 2018 zonal mean at 17 km altitude (**a**) and in vertical distribution for tropical regions 20° S–20° N (**b**). Maximum and minimum values appear above (dark red) and below (violet) the colour keys, respectively. White: no data.

## C2 Comparison of different volcanic injection inventories

Table C1 shows a comparison of annual volcanic SO<sub>2</sub> emission inventories from Carn et al. (2016) and Mills et al. (2016) with this study.

**Table C1.** Comparison of different volcanic emission inventories (annual SO<sub>2</sub> – kt): volcanic SO<sub>2</sub> emissions reaching the stratosphere and the uppermost tropical troposphere from the Volcanic Sulfur Emission Inventory (Table 2) in this study, ending in August 2019 (+ about 19 MtSO<sub>2</sub> yr<sup>-1</sup> from degassing into the troposphere, Diehl et al., 2012); total annual amount and explosive annual amount of global volcanic SO<sub>2</sub> emissions, calculated from satellite observations in 1979 to 2014 by Carn et al. (2016, their Table 3) and total SO<sub>2</sub> emissions from Mills et al. (2016, their Table S4).

Year	This study: stratospheric	Carn et al. (2016): total	Carn et al. (2016): explosive	Mills et al. (2016): total
1990	744	186	186	50
1991	18 424	26 082	24 214	19 500
1992	794	810	810	600
1993	426	450	450	400
1994	337	1874	360	300
1995	156	TOMS data gap	–	–
1996	436	987	100	860
1997	254	41	41	–
1998	255	3265	38	–
1999	398	130	85	70
2000	185	653	336	520
2001	400	1783	122	34
2002	368	2626	271	160
2003	207	679	679	210
2004	256	2997	410	–
2005	445	4634	2501	610
2006	611	1347	661	3210
2007	450	712	122	130
2008	688	2625	2318	2044
2009	839	1934	1379	1570
2010	424	1470	867	903
2011	689	6030	4310	6930
2012	355	763	563	210
2013	448	185	180	30
2014	716	5296	608	480
2015	993	–	–	–
2016	748	–	–	–
2017	600	–	–	–
2018	881	–	–	–
2019	1149	–	–	–

### C3 Comparison with different case studies for volcanic “point source” injections

To compare the simulations from this study using volcanic SO<sub>2</sub> as a spatially resolved SO<sub>2</sub> cloud instead of the traditional point source approach, some case studies are shown in this chapter. For this purpose, simulations are performed with the same model set-up and with point source injections using the TREXP (Jöckel et al., 2010) sub-model. As case studies we compare different point source injection methods of volcanic SO<sub>2</sub> emissions with the EMAC model simulations using the three-dimensional perturbations and MIPAS Level-2 observations for the Nabro eruption in 2011 and the Sarychev eruption in 2009.

To ensure identical boundary conditions, the point source simulations were started using the identical model set-up, and only the volcanic SO<sub>2</sub> injections differ from those performed in this study. In contrast to the method used in this study, the point source methods always require, additionally to injected total SO<sub>2</sub> mass derived from nadir instruments, assumptions about the altitude range and the duration of the eruption and also the area of the initial plume. In the examples we use the settings of Mills et al. (2016) and the corresponding entries in Table 2. For the latter we assume as one option that the SO<sub>2</sub> mass is injected equally distributed between the latitude-dependent lower minimum altitude given in the caption, and approximately the listed altitude of the maximum perturbation of the mixing ratio, the injection time, and the duration is assumed to be the same as in Mills et al. (2016) or, if missing, in the Smithsonian database. Alternatively we assume that emissions begin about 1.2 km (two to three model layers) above the minimum altitude.

We compare zonal average vertical distributions of SO<sub>2</sub> (Fig. C2) and sulfate (Fig. C3) some weeks after the eruptions for the Sarychev eruption in 2009 (left) and the Nabro eruption in 2011 (right). In the case of using the three-dimensional SO<sub>2</sub> perturbations, the resulting SO<sub>2</sub> distribution is smoother than with direct use of Table 2 for “point sources”. Using Mills “point sources” shifts the SO<sub>2</sub> plume to lower altitudes.

Five-day-average radiative forcing at the TOA is shown in Fig. C4. The black curves correspond to the red curves in Fig. 11. Using the assumptions of Mills et al. (2016) about the vertical distribution of the SO<sub>2</sub> injection leads to less forcing in the case of Nabro and after about 5 weeks after the Sarychev eruption (Fig. C4, red curves). For the latter the peak is stronger since more mass is injected than in the other approaches. It is dominated by contributions from aerosol in the mid- and high-latitude lowermost stratosphere. Using Table 2 leads to approximate agreement if the provided altitude is about the top of the column into which it is injected, using as a bottom about 1.2 km above the latitude-dependent minimum altitude (blue curves). Using the full range leads to an underestimate compared to the simulation using the MIPAS observations directly as three-dimensional SO<sub>2</sub> per-

turbation (light blue curves). This is due to more efficient removal processes in the upper troposphere and the lowermost stratosphere than in the layers above. The lower panel for 2009 also contains a sensitivity study similar to the blue curve but with the eruption of Manda Hararo neglected as done by Mills et al. (2016) (dashed) and one where the top of the injection column for Sarychev was one layer lower than in the case with the light blue curve (purple). These examples show that the altitude of the injection has a large impact on the radiative forcing but also that not only medium-sized eruptions matter. For stratospheric AOD shown in the upper panels of Fig. C4 the difference between the approaches is less than for the forcing in the first weeks after the eruption. Later the SAOD decreases faster with the point source approach, especially the one of Mills et al. (2016), than with our method.

Note that considering only aerosol above the fixed pressure level of 100 hPa for the forcing calculations as we did in earlier studies causes misleading results here.

We further show maps at 16 and 18 km altitude and the corresponding Level-2 MIPAS observations (see Figs. C5 to C6). In the case of Nabro using column emissions of up to about 18 km interaction of chemistry, radiative heating, and dynamics leads to the formation of a lofting anti-cyclonic vortex with elevated concentrations of SO<sub>2</sub> and sulfate above 18 km, propagating westward for several weeks. In Fig. C6 this is visible over the sub-tropical eastern Pacific but is not supported by observations in this case. The phenomenon appears to be similar to the one observed after the 2019/2020 wildfires over the South Pacific (Khaykin et al., 2020).

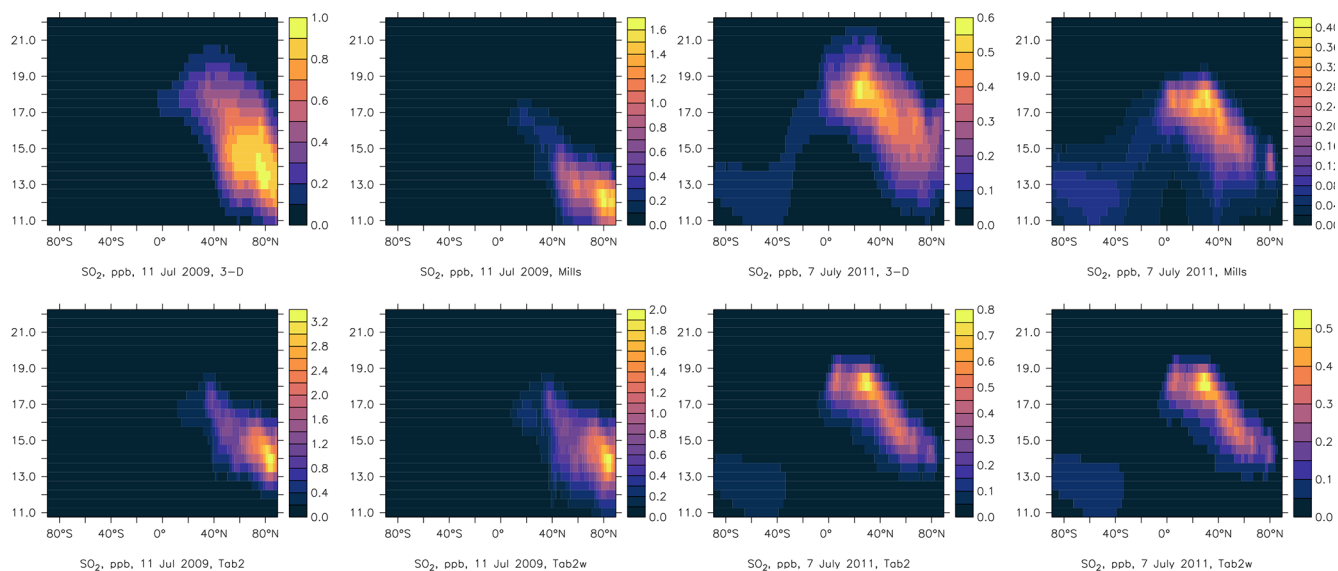


**Figure C2.** Zonal average  $\text{SO}_2$  mixing ratio (ppb) distribution with latitude and altitude (km), 11 July 2009 (four left panels) and 7 July 2011 (four right panels). “3-D” this study, “Mills” emission settings of Mills et al. (2016), “Tab2w” emission in full columns of Table 2, “Tab2” emission starting about 1.2 km above the minimum altitude of Table 2.

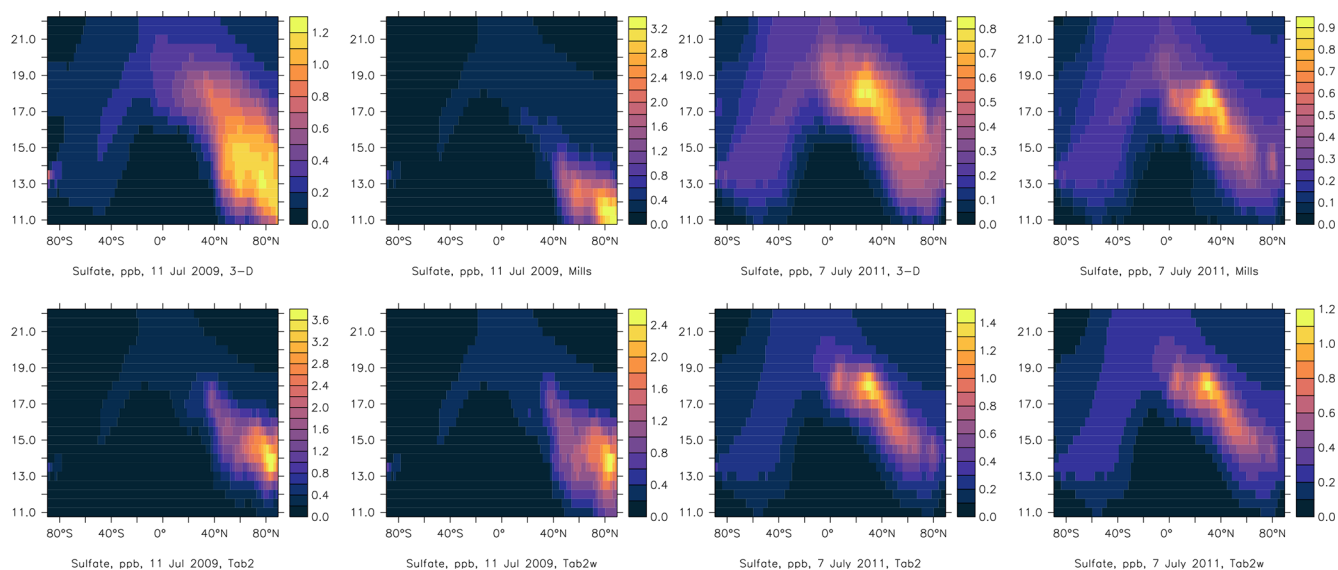


**Figure C3.** Like Fig. C2 but for sulfate in the accumulation mode.

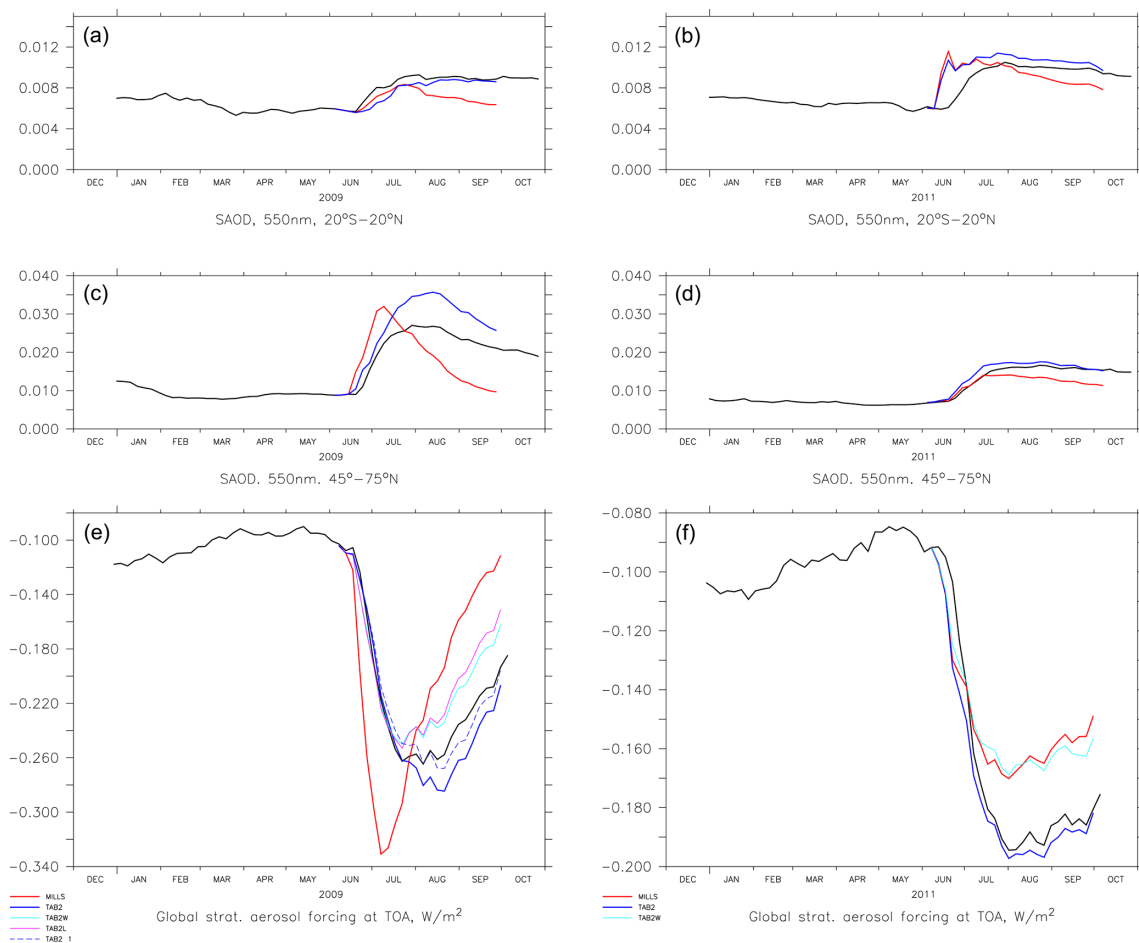


**Figure C4.** Stratospheric AOD (a–d) and global radiative forcing at the TOA (e, f), Sarychev (a, c, e) and Nabro (b, d, f), black line like the red line in Figs. 9 or 11, blue, light blue and purple line “point sources” based on Table 2 with different thicknesses and vertical positions of the column into which this is injected (see text), and red lines with the assumptions of Mills et al. (2016). Dashed blue, light blue, and purple curves: see text.

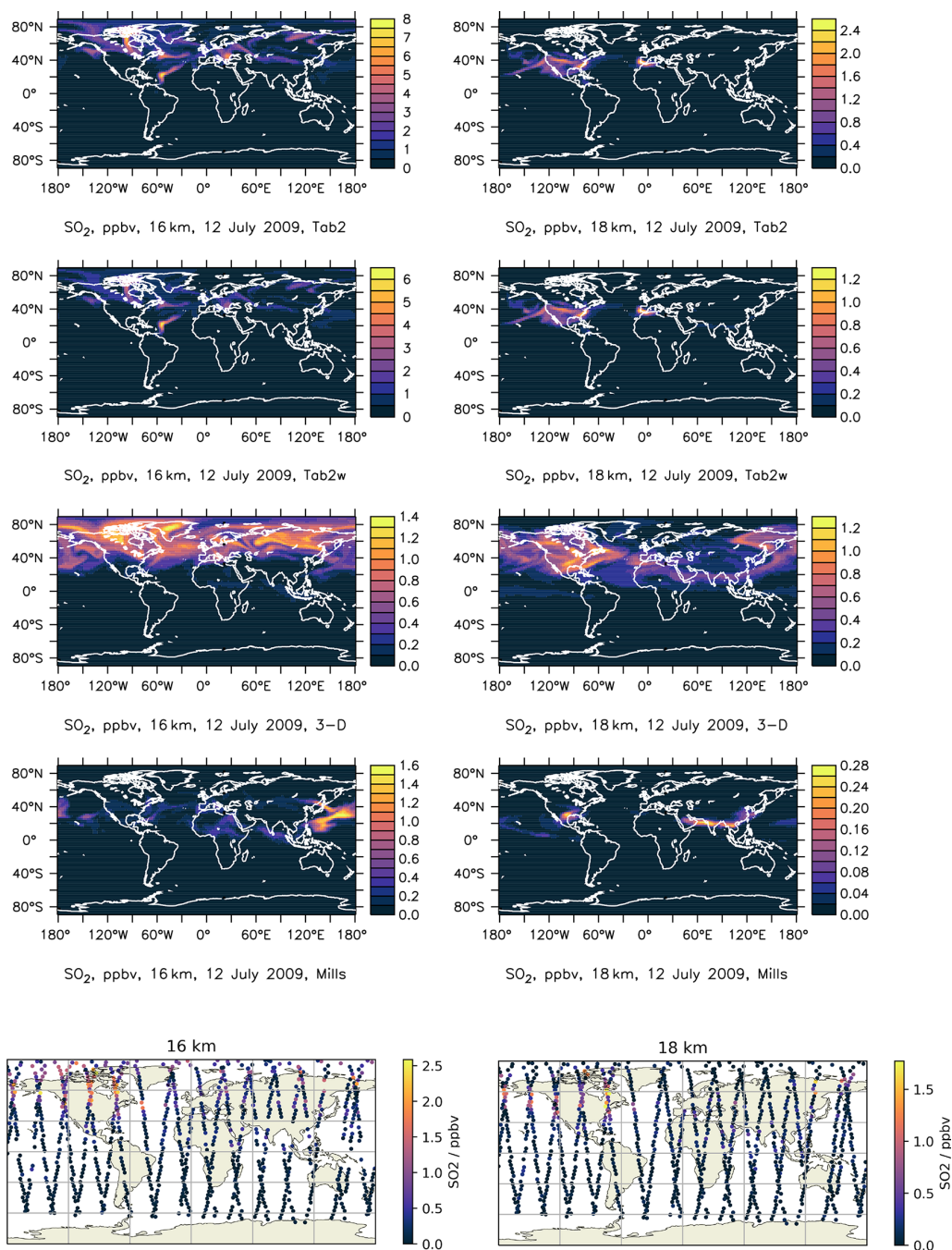


**Figure C5.** SO<sub>2</sub> mixing ratio (ppbv) maps after the Sarychev eruption at 16 km (left column) and 18 km (right column) for point sources of Table 2 in the column between 15 and 17 km (first row), the column between 13 and 17 km (second row), our three-dimensional approach (third row) and the point source assumption of Mills et al. (2016) with a column below 15 km (Manda Hararo neglected) (fourth row). Bottom row from MIPAS observations.

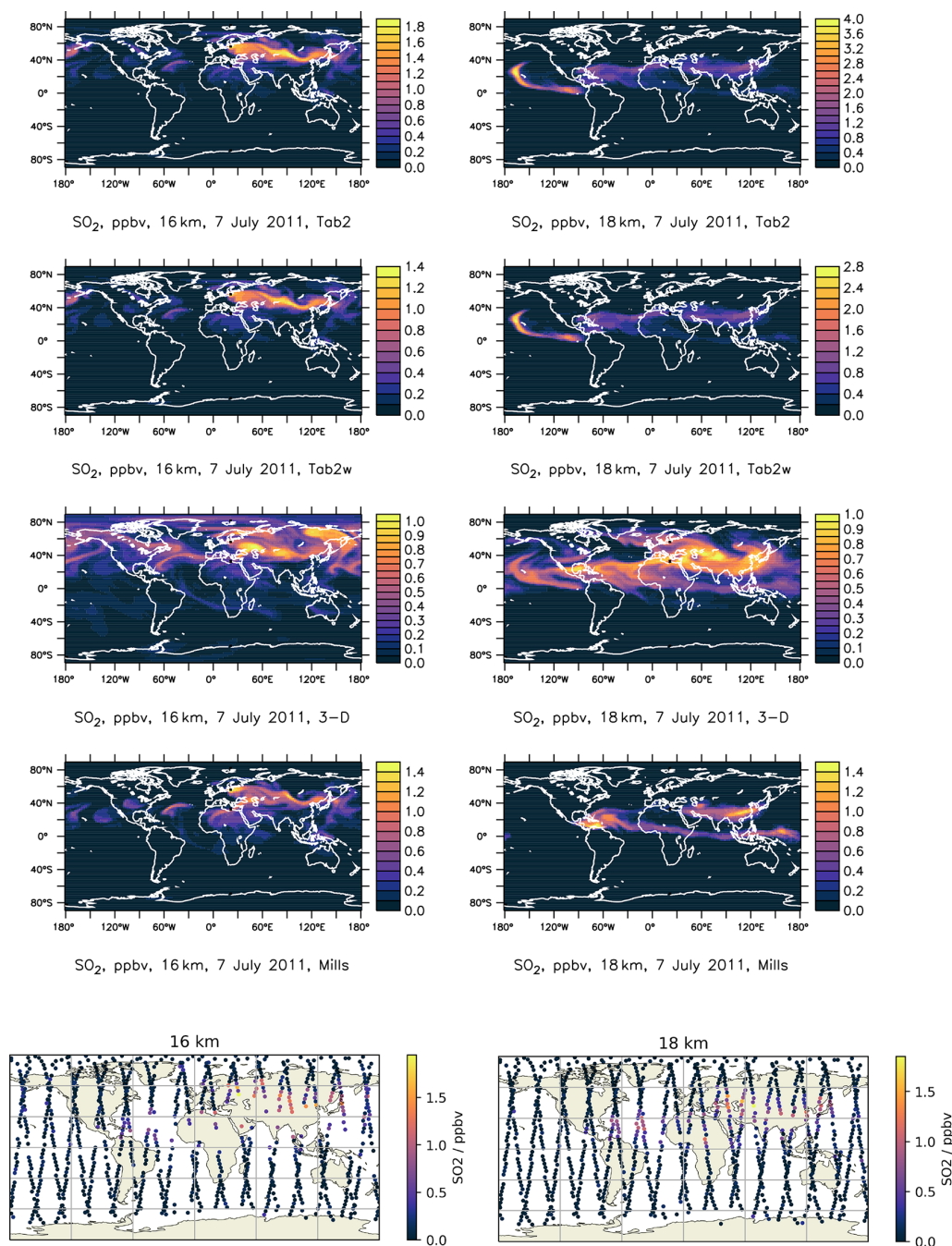


**Figure C6.** SO<sub>2</sub> mixing ratio (ppbv) maps after the Nabro eruption at 16 km (left column) and 18 km (right column) for the point source of Table 2 in the column between 15.5 and 18 km (first row), the column between 14 and 18 km (second row), our three-dimensional approach (third row) and the point source assumption of Mills et al. (2016) with a column below 16 km (fourth row). Bottom row from MIPAS observations.

**Code and data availability.** The Modular Earth Submodel System (MESSy) is continuously developed and used by a consortium of institutions. The use of MESSy and access to the source code is licensed to all affiliates of institutions which are members of the MESSy consortium. Institutions can become a member of the MESSy consortium by signing the MESSy Memorandum of Understanding. More information can be found on the MESSy consortium website (<https://messy-interface.org>, last access: 21 December 2022). The code used here is based on MESSy version 2.52 stored at DKRZ and available from the authors on request. The input data files and model output of EMAC used here are stored at DKRZ, Hamburg, the volcanic inventory and the output for instantaneous radiative forcing at tropopause also at WDCC ([https://doi.org/10.26050/WDC/SSIRC\\_3](https://doi.org/10.26050/WDC/SSIRC_3), Brühl et al., 2021). For the MIPAS data we refer to <http://www.imk-asf.kit.edu/english/308.php> (MIPAS, 2023). A detailed documentation on the used data for MIPAS, SAGE, OSIRIS and GOMOS for the individual events is available from the authors on request.

**Supplement.** The supplement related to this article is available online at: <https://doi.org/10.5194/acp-23-1169-2023-supplement>.

**Author contributions.** JS, CBr and JL defined the scientific questions and scope of this work. JS and CBr conceived the idea and methodology used in this paper and carried out the model simulations and the analysis. MH provided the MIPAS data, CBi provided the GOMOS data, and LR provided the OSIRIS data. All the authors participated in the scientific discussion in regard to satellite data in particular. JS wrote the manuscript, and all the authors reviewed the manuscript and provided advice on the manuscript and figures.

**Competing interests.** The contact author has declared that none of the authors has any competing interests.

**Disclaimer.** Publisher's note: Copernicus Publications remains neutral with regard to jurisdictional claims in published maps and institutional affiliations.

**Special issue statement.** This article is part of the special issue "The Modular Earth Submodel System (MESSy) (ACP/GMD inter-journal SI)". It is not associated with a conference.

**Acknowledgements.** There is a close collaboration within the SPARC/SSIRC (Stratosphere-troposphere Processes And their Role in Climate/Stratospheric Sulfur and its Role in Climate) stratospheric aerosol model intercomparison project (<http://www.sparc-ssirc.org>, last access: 21 December 2022) concerning SO<sub>2</sub> injections derived from satellite data and model intercomparisons. Many thanks to Matthias Kohl for helping to set up the additional point-source emission simulations. The computations have been performed at the Mistral and Levante supercomputers at DKRZ,

Hamburg, Germany. We thank Adam Bourassa, Larry Thomason and the GOMOS, MIPAS, OSIRIS, SAGE, the Copernicus Climate Change Service (projects C3S\_312a\_Lot5 and C3S\_312b\_Lot2), and EOSDIS (NASA) teams for their productive cooperation and providing their satellite datasets. GloSSAC (V2) data were obtained from the NASA Langley Research Center – Atmospheric Sciences Data Center. For the SO<sub>2</sub> inventory we also utilized the NASA SO<sub>2</sub> database at GSFC (<http://so2.gsfc.nasa.gov>, last access: 21 December 2022) for OMI and TOMS and the Smithsonian volcano database (<http://www.volcano.si.edu>, last access: 21 December 2022) We are grateful to our colleagues from the EMAC community and all other MESSy developers and users for their support. We thank Anja Schmidt for editing our paper and providing the data of her paper for comparisons with our results. We would also like to thank the referees for their comments to help us improving our paper.

**Financial support.** The research leading to these results has received funding from the European Research Council under the European Union's Seventh Framework Programme (FP7/2007–2013)/ERC grant agreement 226144 as part of the StratoClim project and funding from ESA Aerosol CCI (European Space Agency).

The article processing charges for this open-access publication were covered by the Max Planck Society.

**Review statement.** This paper was edited by Anja Schmidt and reviewed by Thomas Aubry and two anonymous referees.

## References

- Andersson, S. M., Martinsson, B. G., Vernier, J.-P., Friberg, J., Brenninkmeijer, C. A. M., Hermann, M., van Velthoven, P. F. J., and Zahn, A.: Significant radiative impact of volcanic aerosol in the lowermost stratosphere, *Nat. Commun.*, 6, 7692, <https://doi.org/10.1038/ncomms8692>, 2015.
- Aquila, V., Oman, L. D., Stolarski, R. S., Colarco, P. R., and Newman, P. A.: Dispersion of the volcanic sulfate cloud from a Mount Pinatubo-like eruption, *J. Geophys. Res.-Atmos.*, 117, D06216, <https://doi.org/10.1029/2011JD016968>, 2012.
- Astitha, M., Lelieveld, J., Abdel Kader, M., Pozzer, A., and de Meij, A.: Parameterization of dust emissions in the global atmospheric chemistry-climate model EMAC: impact of nudging and soil properties, *Atmos. Chem. Phys.*, 12, 11057–11083, <https://doi.org/10.5194/acp-12-11057-2012>, 2012.
- Aubry, T. J., Staunton-Sykes, J., Marshall, L. R., Haywood, J., Abraham, N. L., and Schmidt, A.: Climate change modulates the stratospheric volcanic sulfate aerosol lifecycle and radiative forcing from tropical eruptions, *Nat. Commun.*, 12, 1–16, <https://doi.org/10.1038/s41467-021-24943-7>, 2021.
- Bertaux, J. L., Kyrölä, E., Fussen, D., Hauchecorne, A., Dalaudier, F., Sofieva, V., Tamminen, J., Vanhellefont, F., Fanton d'Andon, O., Barrot, G., Mangin, A., Blanot, L., Lebrun, J. C., Pérot, K., Fehr, T., Saavedra, L., Leppelmeier, G. W., and Fraisse, R.: Global ozone monitoring by occultation of stars: an overview

- of GOMOS measurements on ENVISAT, *Atmos. Chem. Phys.*, 10, 12091–12148, <https://doi.org/10.5194/acp-10-12091-2010>, 2010.
- Bingen, C., Robert, C. E., Stebel, K., Brühl, C., Schallock, J., Vanhellemont, F., Matshvili, N., Höpfner, M., Trickl, T., Barnes, J. E., Jumelet, J., Vernier, J.-P., Popp, T., de Leeuw, G., and Pinnock, S.: Stratospheric aerosol data records for the climate change initiative: Development, validation and application to chemistry-climate modelling, *Remote Sens. Environ.*, 203, 296–321, <https://doi.org/10.1016/j.rse.2017.06.002>, 2017.
- Bingen, C., Robert, C., Hermans, C., Vanhellemont, F., Matshvili, N., Dekemper, E., and Fussen, D.: A Revised Cross-Section Database for Gas Retrieval in the UV-Visible-Near IR Range, Applied to the GOMOS Retrieval Algorithm AerGOM, *Front. Environ. Sci.*, 7, 1–18, <https://doi.org/10.3389/fenvs.2019.00118>, 2019.
- Boucher, O.: *Atmospheric Aerosols*, Springer Netherlands, Dordrecht, <https://doi.org/10.1007/978-94-017-9649-1>, 2015.
- Bourassa, A. E., Rieger, L. A., Lloyd, N. D., and Degenstein, D. A.: Odin-OSIRIS stratospheric aerosol data product and SAGE III intercomparison, *Atmos. Chem. Phys.*, 12, 605–614, <https://doi.org/10.5194/acp-12-605-2012>, 2012a.
- Bourassa, A. E., Robock, A., Randel, W. J., Deshler, T., Rieger, L. A., Lloyd, N. D., Llewellyn, E. J., and Degenstein, D. A.: Large volcanic aerosol load in the stratosphere linked to Asian monsoon transport, *Science*, 336, 78–81, <https://doi.org/10.1126/science.1219371>, 2012b.
- Brühl, C.: Volcanic SO<sub>2</sub> data derived from limb viewing satellites for the lower stratosphere from 1998 to 2012, and from nadir viewing satellites for the troposphere, World Data Center for Climate (WDCC) at DKRZ [data set], [https://doi.org/10.1594/WDCC/SSIRC\\_1](https://doi.org/10.1594/WDCC/SSIRC_1), 2018.
- Brühl, C., Lelieveld, J., Tost, H., Höpfner, M., and Glatthor, N.: Stratospheric sulfur and its implications for radiative forcing simulated by the chemistry climate model EMAC, *J. Geophys. Res.*, 120, 2103–2118, <https://doi.org/10.1002/2014JD022430>, 2015.
- Brühl, C., Schallock, J., Klingmüller, K., Robert, C., Bingen, C., Clarisse, L., Heckel, A., North, P., and Rieger, L.: Stratospheric aerosol radiative forcing simulated by the chemistry climate model EMAC using Aerosol CCI satellite data, *Atmos. Chem. Phys.*, 18, 12845–12857, <https://doi.org/10.5194/acp-18-12845-2018>, 2018.
- Brühl, C., Schallock, J., and Diehl, T.: Volcanic SO<sub>2</sub> data derived from limb viewing satellites for the lower stratosphere from 1990 to 2019, and from nadir viewing satellites for the troposphere, including the corresponding radiative forcing computed by the CCM EMAC, World Data Center for Climate (WDCC) at DKRZ [data set], [https://doi.org/10.26050/WDCC/SSIRC\\_3](https://doi.org/10.26050/WDCC/SSIRC_3), 2021.
- Carn, S. A., Clarisse, L., and Prata, A. J.: Multi-decadal satellite measurements of global volcanic degassing, *J. Volcanol. Geoth. Res.*, 311, 99–134, <https://doi.org/10.1016/j.jvolgeores.2016.01.002>, 2016.
- Clarisse, L., Coheur, P.-F., Theys, N., Hurtmans, D., and Clerbaux, C.: The 2011 Nabro eruption, a SO<sub>2</sub> plume height analysis using IASI measurements, *Atmos. Chem. Phys.*, 14, 3095–3111, <https://doi.org/10.5194/acp-14-3095-2014>, 2014.
- Crutzen, P. J.: The possible importance of CSO for the sulfate layer of the stratosphere, *Geophys. Res. Lett.*, 3, 73–76, <https://doi.org/10.1029/GL0031002p00073>, 1976.
- Dhomse, S. S., Emmerson, K. M., Mann, G. W., Bellouin, N., Carslaw, K. S., Chipperfield, M. P., Hommel, R., Abraham, N. L., Telford, P., Braesicke, P., Dalvi, M., Johnson, C. E., O'Connor, F., Morgenstern, O., Pyle, J. A., Deshler, T., Zawodny, J. M., and Thomason, L. W.: Aerosol microphysics simulations of the Mt. Pinatubo eruption with the UM-UKCA composition-climate model, *Atmos. Chem. Phys.*, 14, 11221–11246, <https://doi.org/10.5194/acp-14-11221-2014>, 2014.
- Diehl, T., Heil, A., Chin, M., Pan, X., Streets, D., Schultz, M., and Kinne, S.: Anthropogenic, biomass burning, and volcanic emissions of black carbon, organic carbon, and SO<sub>2</sub> from 1980 to 2010 for hindcast model experiments, *Atmos. Chem. Phys. Discuss.*, 12, 24895–24954, <https://doi.org/10.5194/acpd-12-24895-2012>, 2012.
- Dietmüller, S., Jöckel, P., Tost, H., Kunze, M., Gellhorn, C., Brinkop, S., Frömming, C., Ponater, M., Steil, B., Lauer, A., and Hendricks, J.: A new radiation infrastructure for the Modular Earth Submodel System (MESSy, based on version 2.51), *Geosci. Model Dev.*, 9, 2209–2222, <https://doi.org/10.5194/gmd-9-2209-2016>, 2016.
- English, J. M., Toon, O. B., and Mills, M. J.: Microphysical simulations of large volcanic eruptions: Pinatubo and Toba, *J. Geophys. Res.-Atmos.*, 118, 1880–1895, <https://doi.org/10.1002/jgrd.50196>, 2013.
- Fairlie, T. D., Vernier, J.-P., Natarajan, M., and Bedka, K. M.: Dispersion of the Nabro volcanic plume and its relation to the Asian summer monsoon, *Atmos. Chem. Phys.*, 14, 7045–7057, <https://doi.org/10.5194/acp-14-7045-2014>, 2014.
- Fasullo, J. T., Tomas, R., Stevenson, S., Otto-Bliesner, B., Brady, E., and Wahl, E.: The amplifying influence of increased ocean stratification on a future year without a summer, *Nat. Commun.*, 8, 1–10, <https://doi.org/10.1038/s41467-017-01302-z>, 2017.
- Fischer, H., Birk, M., Blom, C., Carli, B., Carlotti, M., von Clarmann, T., Delbouille, L., Dudhia, A., Ehalt, D., Endemann, M., Flaud, J. M., Gessner, R., Kleinert, A., Koopman, R., Langen, J., López-Puertas, M., Mosner, P., Nett, H., Oelhaf, H., Perron, G., Remedios, J., Ridolfi, M., Stiller, G., and Zander, R.: MI-PAS: an instrument for atmospheric and climate research, *Atmos. Chem. Phys.*, 8, 2151–2188, <https://doi.org/10.5194/acp-8-2151-2008>, 2008.
- Friberg, J., Martinsson, B. G., Andersson, S. M., and Sandvik, O. S.: Volcanic impact on the climate – the stratospheric aerosol load in the period 2006–2015, *Atmos. Chem. Phys.*, 18, 11149–11169, <https://doi.org/10.5194/acp-18-11149-2018>, 2018.
- Fromm, M., Peterson, D., and Di Girolamo, L.: The Primary Convective Pathway for Observed Wildfire Emissions in the Upper Troposphere and Lower Stratosphere: A Targeted Reinterpretation, *J. Geophys. Res.-Atmos.*, 124, 13254–13272, <https://doi.org/10.1029/2019JD031006>, 2019.
- Giorgetta, M. A., Manzini, E., and Roeckner, E.: Forcing of the quasi-biennial oscillation from a broad spectrum of atmospheric waves, *Geophys. Res. Lett.*, 29, 86-1–86-4, <https://doi.org/10.1029/2002GL014756>, 2002.
- Giorgetta, M. A., Manzini, E., Roeckner, E., Esch, M., and Bengtsson, L.: Climatology and forcing of the quasi-biennial oscillation in the MAECHAM5 model, *J. Climate*, 19, 3882–3901, <https://doi.org/10.1175/JCLI3830.1>, 2006.
- Glantz, P., Bourassa, A., Herber, A., Iversen, T., Karlsson, J., Kirkevåg, A., Maturilli, M., Seland, Ø., Stebel, K., Struthers,

- H., Tesche, M., and Thomason, L.: Remote sensing of aerosols in the Arctic for an evaluation of global climate model simulations, *J. Geophys. Res.-Atmos.*, 119, 8169–8188, <https://doi.org/10.1002/2013JD021279>, 2014.
- Glatthor, N., Höpfner, M., Baker, I. T., Berry, J., Campbell, J. E., Kawa, S. R., Krysztofiak, G., Leyser, A., Sinnhuber, B.-M., Stiller, G. P., Stinecipher, J., and Von Clarmann, T.: Tropical sources and sinks of carbonyl sulfide observed from space, *Geophys. Res. Lett.*, 42, 10082–10090, <https://doi.org/10.1002/2015GL066293>, 2015.
- Glatthor, N., Höpfner, M., Leyser, A., Stiller, G. P., von Clarmann, T., Grabowski, U., Kellmann, S., Linden, A., Sinnhuber, B.-M., Krysztofiak, G., and Walker, K. A.: Global carbonyl sulfide (OCS) measured by MIPAS/Envisat during 2002–2012, *Atmos. Chem. Phys.*, 17, 2631–2652, <https://doi.org/10.5194/acp-17-2631-2017>, 2017.
- Grainger, R. G., Lambert, A., Rodgers, C. D., Taylor, F. W., and Deshler, T.: Stratospheric aerosol effective radius, surface area and volume estimated from infrared measurements, *J. Geophys. Res.*, 100, 16507–16518, <https://doi.org/10.1029/95JD00988>, 1995.
- Guo, S., Bluth, G. J., Rose, W. I., Watson, I. M., and Prata, A. J.: Re-evaluation of SO<sub>2</sub> release of the 15 June 1991 Pinatubo eruption using ultraviolet and infrared satellite sensors, *Geochem. Geophys. Geosy.*, 5, 1–31, <https://doi.org/10.1029/2003GC000654>, 2004.
- Hansen, J., Sato, M., Ruedy, R., Nazarenko, L., Lacis, A., Schmidt, G. A., Russell, G., Aleinov, I., Bauer, M., Bauer, S., Bell, N., Cairns, B., Canuto, V., Chandler, M., Cheng, Y., Del Genio, A., Faluvegi, G., Fleming, E., Friend, A., Hall, T., Jackman, C., Kelley, M., Kiang, N., Koch, D., Lean, J., Lerner, J., Lo, K., Menon, S., Miller, R., Minnis, P., Novakov, T., Oinas, V., Perlwitz, J., Perlwitz, J., Rind, D., Romanou, A., Shindell, D., Stone, P., Sun, S., Tausnev, N., Thresher, D., Wielicki, B., Wong, T., Yao, M., and Zhang, S.: Efficacy of climate forcings, *J. Geophys. Res.-Atmos.*, 110, 1–45, <https://doi.org/10.1029/2005JD005776>, 2005.
- Höpfner, M., Glatthor, N., Grabowski, U., Kellmann, S., Kiefer, M., Linden, A., Orphal, J., Stiller, G., von Clarmann, T., Funke, B., and Boone, C. D.: Sulfur dioxide (SO<sub>2</sub>) as observed by MIPAS/Envisat: temporal development and spatial distribution at 15–45 km altitude, *Atmos. Chem. Phys.*, 13, 10405–10423, <https://doi.org/10.5194/acp-13-10405-2013>, 2013.
- Höpfner, M., Boone, C. D., Funke, B., Glatthor, N., Grabowski, U., Günther, A., Kellmann, S., Kiefer, M., Linden, A., Losow, S., Pumphrey, H. C., Read, W. G., Roiger, A., Stiller, G., Schlager, H., von Clarmann, T., and Wissmüller, K.: Sulfur dioxide (SO<sub>2</sub>) from MIPAS in the upper troposphere and lower stratosphere 2002–2012, *Atmos. Chem. Phys.*, 15, 7017–7037, <https://doi.org/10.5194/acp-15-7017-2015>, 2015.
- IPCC: 2013: Climate Change 2013: The Physical Science Basis. Contribution of Working Group I to the Fifth Assessment Report of the Intergovernmental Panel on Climate Change, edited by: Stocker, T. F., Qin, D., Plattner, G.-K., Tignor, M., Allen, S. K., Boschung, J., Nauels, A., Xia, Y., Bex, V., and Midgley, P. M., Cambridge University Press, Cambridge, United Kingdom and New York, NY, USA, <https://doi.org/10.1017/CBO9781107415324>, 2013.
- Jöckel, P., Sander, R., Kerkweg, A., Tost, H., and Lelieveld, J.: Technical Note: The Modular Earth Submodel System (MESSy) – a new approach towards Earth System Modeling, *Atmos. Chem. Phys.*, 5, 433–444, <https://doi.org/10.5194/acp-5-433-2005>, 2005.
- Jöckel, P., Tost, H., Pozzer, A., Brühl, C., Buchholz, J., Ganzeveld, L., Hoor, P., Kerkweg, A., Lawrence, M. G., Sander, R., Steil, B., Stiller, G., Tanarhte, M., Taraborrelli, D., van Aardenne, J., and Lelieveld, J.: The atmospheric chemistry general circulation model ECHAM5/MESSy1: consistent simulation of ozone from the surface to the mesosphere, *Atmos. Chem. Phys.*, 6, 5067–5104, <https://doi.org/10.5194/acp-6-5067-2006>, 2006.
- Jöckel, P., Kerkweg, A., Pozzer, A., Sander, R., Tost, H., Riede, H., Baumgaertner, A., Gromov, S., and Kern, B.: Development cycle 2 of the Modular Earth Submodel System (MESSy2), *Geosci. Model Dev.*, 3, 717–752, <https://doi.org/10.5194/gmd-3-717-2010>, 2010.
- Kerkweg, A.: Global Modelling of Atmospheric Halogen Chemistry in the Marine Boundary Layer, PhD thesis, Friedrich-Wilhelms-Universität Bonn, <https://nbn-resolving.org/urn:nbn:de:hbz:5N-06365> (last access: 11 January 2023), 2005.
- Kerkweg, A., Buchholz, J., Ganzeveld, L., Pozzer, A., Tost, H., and Jöckel, P.: Technical Note: An implementation of the dry removal processes DRY DEPosition and SEDimentation in the Modular Earth Submodel System (MESSy), *Atmos. Chem. Phys.*, 6, 4617–4632, <https://doi.org/10.5194/acp-6-4617-2006>, 2006a.
- Kerkweg, A., Sander, R., Tost, H., and Jöckel, P.: Technical note: Implementation of prescribed (OFFLEM), calculated (ONLEM), and pseudo-emissions (TNUDGE) of chemical species in the Modular Earth Submodel System (MESSy), *Atmos. Chem. Phys.*, 6, 3603–3609, <https://doi.org/10.5194/acp-6-3603-2006>, 2006b.
- Kettle, A. J. and Andreae, M. O.: Flux of dimethylsulfide from the oceans: A comparison of updated data sets and flux models, *J. Geophys. Res.*, 105, 26793–26808, <https://doi.org/10.1029/2000JD900252>, 2000.
- Khaykin, S., Legras, B., Bucci, S., Sellitto, P., Isaksen, I., Tencé, F., Bekki, S., Bourassa, A., Rieger, L., Zawada, D., Jumelet, J., and Godin-Beekmann, S.: The 2019/20 Australian wildfires generated a persistent smoke-charged vortex rising up to 35 km altitude, *Commun. Earth Environ.*, 1, 1–12, <https://doi.org/10.1038/s43247-020-00022-5>, 2020.
- Klingmüller, K., Metzger, S., Abdelkader, M., Karydis, V. A., Stenichkov, G. L., Pozzer, A., and Lelieveld, J.: Revised mineral dust emissions in the atmospheric chemistry–climate model EMAC (MESSy 2.52 DU\_Astithal KKDU2017 patch), *Geosci. Model Dev.*, 11, 989–1008, <https://doi.org/10.5194/gmd-11-989-2018>, 2018.
- Kloss, C., Berthet, G., Sellitto, P., Ploeger, F., Bucci, S., Khaykin, S., Jégou, F., Taha, G., Thomason, L. W., Barret, B., Le Flochmoen, E., von Hobe, M., Bossolasco, A., Bègue, N., and Legras, B.: Transport of the 2017 Canadian wildfire plume to the tropics via the Asian monsoon circulation, *Atmos. Chem. Phys.*, 19, 13547–13567, <https://doi.org/10.5194/acp-19-13547-2019>, 2019.
- Kloss, C., Berthet, G., Sellitto, P., Ploeger, F., Taha, G., Tidiga, M., Eremenko, M., Bossolasco, A., Jégou, F., Renard, J.-B., and Legras, B.: Stratospheric aerosol layer perturbation caused by the 2019 Raikoke and Ulawun eruptions and their radiative forcing,

- Atmos. Chem. Phys., 21, 535–560, <https://doi.org/10.5194/acp-21-535-2021>, 2021.
- Kovilakam, M., Thomason, L. W., Ernest, N., Rieger, L., Bourassa, A., and Millán, L.: The Global Space-based Stratospheric Aerosol Climatology (version 2.0): 1979–2018, Earth Syst. Sci. Data, 12, 2607–2634, <https://doi.org/10.5194/essd-12-2607-2020>, 2020.
- Kyrölä, E., Tamminen, J., Sofieva, V., Bertaux, J. L., Hauchecorne, A., Dalaudier, F., Fussen, D., Vanhellefont, F., Fanton d’Andon, O., Barrot, G., Guirlet, M., Fehr, T., and Saavedra de Miguel, L.: GOMOS O<sub>3</sub>, NO<sub>2</sub>, and NO<sub>3</sub> observations in 2002–2008, Atmos. Chem. Phys., 10, 7723–7738, <https://doi.org/10.5194/acp-10-7723-2010>, 2010.
- Long, C. S. and Stowe, L. L.: using the NOAA/AVHRR to study stratospheric aerosol optical thicknesses following the Mt. Pinatubo Eruption, Geophys. Res. Lett., 21, 2215–2218, <https://doi.org/10.1029/94GL01322>, 1994.
- McGregor, H. V., Evans, M. N., Goosse, H., Leduc, G., Martrat, B., Addison, J. A., Mortyn, P. G., Oppo, D. W., Seidenkrantz, M. S., Sicre, M. A., Phipps, S. J., Selvaraj, K., Thirumalai, K., Filipsson, H. L., and Ersek, V.: Robust global ocean cooling trend for the pre-industrial Common Era, Nat. Geosci., 8, 671–677, <https://doi.org/10.1038/ngeo2510>, 2015.
- Metzger, S. and Lelieveld, J.: Reformulating atmospheric aerosol thermodynamics and hygroscopic growth into fog, haze and clouds, Atmos. Chem. Phys., 7, 3163–3193, <https://doi.org/10.5194/acp-7-3163-2007>, 2007.
- Mills, M. J., Schmidt, A., Easter, R., Solomon, S., Kinnison, D. E., Ghan, S. J., Neely, R. R., Marsh, D. R., Conley, A., Bardeen, C. G., and Gettelman, A.: Global volcanic aerosol properties derived from emissions, 1990–2014, using CESM1(WACCM), J. Geophys. Res.-Atmos., 121, 2332–2348, <https://doi.org/10.1002/2015JD024290>, 2016.
- Minnis, P., Harrison, E. F., Stowe, L. L., Gibson, G. G., Denn, F. M., Doelling, D. R., and Smith, W. L.: Radiative climate forcing by the Mount Pinatubo eruption, Science, 259, 1411–1415, <https://doi.org/10.1126/science.259.5100.1411>, 1993.
- MIPAS: MIPAS/Envisat, MIPAS [data set], <https://www.imk-asf.kit.edu/english/308.php>, last access: 11 January 2023.
- Nordeng, T. E.: Extended version of the convective parametrization scheme at ECMWF and their impact on the mean and transient activity of the model in the tropics, ECMWF Tech. Memo., no. 206, 09/1994, <https://doi.org/10.21957/e34xwhysw>, 1994.
- Pozzer, A., Jöckel, P., Sander, R., Williams, J., Ganzeveld, L., and Lelieveld, J.: Technical Note: The MESSy-submodel AIRSEA calculating the air-sea exchange of chemical species, Atmos. Chem. Phys., 6, 5435–5444, <https://doi.org/10.5194/acp-6-5435-2006>, 2006.
- Pringle, K. J., Tost, H., Message, S., Steil, B., Giannadaki, D., Nenes, A., Fountoukis, C., Stier, P., Vignati, E., and Lelieveld, J.: Description and evaluation of GMXe: a new aerosol submodel for global simulations (v1), Geosci. Model Dev., 3, 391–412, <https://doi.org/10.5194/gmd-3-391-2010>, 2010.
- Ridley, D. A., Solomon, S., Barnes, J. E., Burlakov, V. D., Deshler, T., Dolgii, S. I., Herber, A. B., Nagai, T., Neely, R. R., Nevzorov, A. V., Ritter, C., Sakai, T., Santer, B. D., Sato, M., Schmidt, A., Uchino, O., and Vernier, J. P.: Total volcanic stratospheric aerosol optical depths and implications for global climate change, Geophys. Res. Lett., 41, 7763–7769, <https://doi.org/10.1002/2014GL061541>, 2014.
- Rieger, L. A., Bourassa, A. E., and Degenstein, D. A.: Merging the OSIRIS and SAGE II stratospheric aerosol records, J. Geophys. Res., 120, 8890–8904, <https://doi.org/10.1002/2015JD023133>, 2015.
- Rieger, L. A., Malinina, E. P., Rozanov, A. V., Burrows, J. P., Bourassa, A. E., and Degenstein, D. A.: A study of the approaches used to retrieve aerosol extinction, as applied to limb observations made by OSIRIS and SCIAMACHY, Atmos. Meas. Tech., 11, 3433–3445, <https://doi.org/10.5194/amt-11-3433-2018>, 2018.
- Rieger, L. A., Zawada, D. J., Bourassa, A. E., and Degenstein, D. A.: A Multiwavelength Retrieval Approach for Improved OSIRIS Aerosol Extinction Retrievals, J. Geophys. Res.-Atmos., 124, 2018JD029897, <https://doi.org/10.1029/2018JD029897>, 2019.
- Rieger, L. A., Cole, J. N. S., Fyfe, J. C., Po-Chedley, S., Cameron-Smith, P. J., Durack, P. J., Gillett, N. P., and Tang, Q.: Quantifying CanESM5 and EAMv1 sensitivities to Mt. Pinatubo volcanic forcing for the CMIP6 historical experiment, Geosci. Model Dev., 13, 4831–4843, <https://doi.org/10.5194/gmd-13-4831-2020>, 2020.
- Rinsland, C. P., Gunson, M. R., Ko, M. K., Weisenstein, D. W., Zander, R., Abrams, M. C., Goldman, A., Sze, N. D., and Yue, G. K.: H<sub>2</sub>SO<sub>4</sub> photolysis: A source of sulfur dioxide in the upper stratosphere, Geophys. Res. Lett., 22, 1109–1112, <https://doi.org/10.1029/95GL00917>, 1995.
- Robert, C. É., Bingen, C., Vanhellefont, F., Matshvili, N., Dekemper, E., Tétard, C., Fussen, D., Bourassa, A., and Zehner, C.: AER-GOM, an improved algorithm for stratospheric aerosol extinction retrieval from GOMOS observations – Part 2: Intercomparisons, Atmos. Meas. Tech., 9, 4701–4718, <https://doi.org/10.5194/amt-9-4701-2016>, 2016.
- Roeckner, E., Bäuml, G., Bonaventura, L., Brokopf, R., Esch, M., Giorgetta, M., Hagemann, S., Kirchner, I., Kornblüeh, L., Manzini, E., Rhodin, A., Schlese, U., Schulzweida, U., and Tompkins, A.: The atmospheric general circulation model ECHAM 5. PART I: Model description, Max-Planck-Institut für Meteorologie Number, 349, <http://hdl.handle.net/11858/00-001M-0000-0012-0144-5> (last access: 11 January 2023) 2003.
- Roeckner, E., Brokopf, R., Esch, M., Giorgetta, M. A., Hagemann, S., Kornblüeh, L., Manzini, E., Schlese, U., and Schulzweida, U.: Sensitivity of simulated climate to horizontal and vertical resolution in the ECHAM5 atmosphere model, J. Climate, 19, 3771–3791, <https://doi.org/10.1175/JCLI3824.1>, 2006.
- Sander, R., Baumgaertner, A., Gromov, S., Harder, H., Jöckel, P., Kerkweg, A., Kubistin, D., Regelin, E., Riede, H., Sandu, A., Taraborrelli, D., Tost, H., and Xie, Z.-Q.: The atmospheric chemistry box model CAABA/MECCA-3.0, Geosci. Model Dev., 4, 373–380, <https://doi.org/10.5194/gmd-4-373-2011>, 2011.
- Santer, B. D., Bonfils, C., Painter, J. F., Zelinka, M. D., Mears, C., Solomon, S., Schmidt, G. A., Fyfe, J. C., Cole, J. N., Nazarenko, L., Taylor, K. E., and Wentz, F. J.: Volcanic contribution to decadal changes in tropospheric temperature, Nat. Geosci., 7, 185–189, <https://doi.org/10.1038/ngeo2098>, 2014.
- Schmidt, A., Mills, M. J., Ghan, S., Gregory, J. M., Allan, R. P., Andrews, T., Bardeen, C. G., Conley, A.,

- Forster, P. M., Gettelman, A., Portmann, R. W., Solomon, S., and Toon, O. B.: Volcanic Radiative Forcing From 1979 to 2015, *J. Geophys. Res.-Atmos.*, 123, 12491–12508, <https://doi.org/10.1029/2018JD028776>, 2018.
- Sellitto, P., Belhadji, R., Kloss, C., and Legras, B.: Radiative impacts of the Australian bushfires 2019–2020 – Part 1: Large-scale radiative forcing, *Atmos. Chem. Phys.*, 22, 9299–9311, <https://doi.org/10.5194/acp-22-9299-2022>, 2022.
- Solomon, S., Daniel, J. S., Neely, R. R., Vernier, J.-P., Dutton, E. G., and Thomason, L. W.: The persistently variable “background” stratospheric aerosol layer and global climate change, *Science*, 333, 866–870, <https://doi.org/10.1126/science.1206027>, 2011.
- Stier, P., Feichter, J., Kinne, S., Kloster, S., Vignati, E., Wilson, J., Ganzeveld, L., Tegen, I., Werner, M., Balkanski, Y., Schulz, M., Boucher, O., Minikin, A., and Petzold, A.: The aerosol-climate model ECHAM5-HAM, *Atmos. Chem. Phys.*, 5, 1125–1156, <https://doi.org/10.5194/acp-5-1125-2005>, 2005.
- Swindles, G. T., Savov, I. P., Schmidt, A., Hooper, A., Connor, C. B., and Carrivick, J. L.: Climatic control on Icelandic volcanic activity during the mid-Holocene: REPLY, *Geology*, 46, 47–50, <https://doi.org/10.1130/G40290Y.1>, 2018.
- Thomason, L. W., Burton, S. P., Luo, B.-P., and Peter, T.: SAGE II measurements of stratospheric aerosol properties at non-volcanic levels, *Atmos. Chem. Phys.*, 8, 983–995, <https://doi.org/10.5194/acp-8-983-2008>, 2008.
- Thomason, L. W., Ernest, N., Millán, L., Rieger, L., Bourassa, A., Vernier, J.-P., Manney, G., Luo, B., Arfeuille, F., and Peter, T.: A global space-based stratospheric aerosol climatology: 1979–2016, *Earth Syst. Sci. Data*, 10, 469–492, <https://doi.org/10.5194/essd-10-469-2018>, 2018.
- Tiedtke, M.: A Comprehensive Mass Flux Scheme for Cumulus Parameterization in Large-Scale Models, *Mon. Weather Rev.*, 117, 1779–1800, [https://doi.org/10.1175/1520-0493\(1989\)117<1779:ACMFSF>2.0.CO;2](https://doi.org/10.1175/1520-0493(1989)117<1779:ACMFSF>2.0.CO;2), 1989.
- Timmreck, C.: Modeling the climatic effects of large explosive volcanic eruptions, *WIREs Clim. Change*, 3, 545–564, <https://doi.org/10.1002/wcc.192>, 2012.
- Timmreck, C., Graf, H. F., and Feichter, J.: Simulation of Mt. Pinatubo volcanic aerosol with the Hamburg climate model ECHAM4, *Theor. Appl. Climatol.*, 62, 85–108, <https://doi.org/10.1007/s007040050076>, 1999.
- Timmreck, C., Mann, G. W., Aquila, V., Hommel, R., Lee, L. A., Schmidt, A., Brühl, C., Carn, S., Chin, M., Dhomse, S. S., Diehl, T., English, J. M., Mills, M. J., Neely, R., Sheng, J., Toohey, M., and Weisenstein, D.: The Interactive Stratospheric Aerosol Model Intercomparison Project (ISA-MIP): motivation and experimental design, *Geosci. Model Dev.*, 11, 2581–2608, <https://doi.org/10.5194/gmd-11-2581-2018>, 2018.
- Toohey, M., Krüger, K., Niemeier, U., and Timmreck, C.: The influence of eruption season on the global aerosol evolution and radiative impact of tropical volcanic eruptions, *Atmos. Chem. Phys.*, 11, 12351–12367, <https://doi.org/10.5194/acp-11-12351-2011>, 2011.
- Tost, H., Jöckel, P., Kerkweg, A., Sander, R., and Lelieveld, J.: Technical note: A new comprehensive SCAVenging submodel for global atmospheric chemistry modelling, *Atmos. Chem. Phys.*, 6, 565–574, <https://doi.org/10.5194/acp-6-565-2006>, 2006a.
- Tost, H., Jöckel, P., and Lelieveld, J.: Influence of different convection parameterisations in a GCM, *Atmos. Chem. Phys.*, 6, 5475–5493, <https://doi.org/10.5194/acp-6-5475-2006>, 2006b.
- Tost, H., Jöckel, P., and Lelieveld, J.: Lightning and convection parameterisations – uncertainties in global modelling, *Atmos. Chem. Phys.*, 7, 4553–4568, <https://doi.org/10.5194/acp-7-4553-2007>, 2007.
- Tost, H., Lawrence, M. G., Brühl, C., Jöckel, P., The GABRIEL Team, and The SCOUT-O3-DARWIN/ACTIVE Team: Uncertainties in atmospheric chemistry modelling due to convection parameterisations and subsequent scavenging, *Atmos. Chem. Phys.*, 10, 1931–1951, <https://doi.org/10.5194/acp-10-1931-2010>, 2010.
- Vanhellemont, F., Fussen, D., and Bingen, C.: Global one-step inversion of satellite occultation measurements: A practical method, *J. Geophys. Res.*, 109, D09306, <https://doi.org/10.1029/2003JD004168>, 2004.
- Vanhellemont, F., Fussen, D., Mateshvili, N., Tétard, C., Bingen, C., Dekemper, E., Loodts, N., Kyrölä, E., Sofieva, V., Tamminen, J., Hauchecorne, A., Bertaux, J.-L., Dalaudier, F., Blanot, L., Fanton d’Andon, O., Barrot, G., Guirlet, M., Fehr, T., and Saavedra, L.: Optical extinction by upper tropospheric/stratospheric aerosols and clouds: GOMOS observations for the period 2002–2008, *Atmos. Chem. Phys.*, 10, 7997–8009, <https://doi.org/10.5194/acp-10-7997-2010>, 2010.
- Vanhellemont, F., Mateshvili, N., Blanot, L., Robert, C. É., Bingen, C., Sofieva, V., Dalaudier, F., Tétard, C., Fussen, D., Dekemper, E., Kyrölä, E., Laine, M., Tamminen, J., and Zehner, C.: AerGOM, an improved algorithm for stratospheric aerosol extinction retrieval from GOMOS observations – Part 1: Algorithm description, *Atmos. Meas. Tech.*, 9, 4687–4700, <https://doi.org/10.5194/amt-9-4687-2016>, 2016.
- Vehkamäki, H., Kulmala, M., Napari, I., Lehtinen, K. E. J., Timmreck, C., Noppel, M., and Laaksonen, A.: An improved parameterization for sulfuric acid – water nucleation rates for tropospheric and stratospheric conditions, *J. Geophys. Res.*, 107, 1–10, <https://doi.org/10.1029/2002JD002184>, 2002.
- Vernier, J.-P., Thomason, L. W., Pommereau, J.-P. P., Bourassa, A. E., Pelon, J., Garnier, A., Hauchecorne, A., Blanot, L., Trepte, C., Degenstein, D. A., and Vargas, F.: Major influence of tropical volcanic eruptions on the stratospheric aerosol layer during the last decade, *Geophys. Res. Lett.*, 38, 1–8, <https://doi.org/10.1029/2011GL047563>, 2011.
- Vernier, J.-P., Fairlie, T. D., Deshler, T., Natarajan, M., Knepp, T., Foster, K., Wienhold, F. G., Bedka, K. M., Thomason, L., and Trepte, C.: In situ and space-based observations of the Kelud volcanic plume: The persistence of ash in the lower stratosphere, *J. Geophys. Res.-Atmos.*, 121, 104–118, <https://doi.org/10.1002/2016JD025344>, 2016.
- Vignati, E., Wilson, J., and Stier, P.: M7: An efficient size-resolved aerosol microphysics module for large-scale aerosol transport models, *J. Geophys. Res.-Atmos.*, 109, D22202, <https://doi.org/10.1029/2003JD004485>, 2004.
- Wilson, J. C., Lee, S.-H., Reeves, J. M., Brock, C. A., Jonsson, H. H., Laffleur, B. G., Loewenstein, M., Podolske, J., Atlas, E., Boering, K., Toon, G., Fahey, D., Bui, T. P., Diskin, G., and Moore, F.: Steady-state aerosol distributions in the extra-tropical, lower stratosphere and the processes that maintain them, *Atmos. Chem.*

- Phys., 8, 6617–6626, <https://doi.org/10.5194/acp-8-6617-2008>, 2008.
- Wong, T., Wielicki, B. A., Lee, R. B., Smith, G. L., Bush, K. A., and Willis, J. K.: Reexamination of the observed decadal variability of the earth radiation budget using altitude-corrected ERBE/ERBS nonscanner WFOV data, *J. Climate*, 19, 4028–4048, <https://doi.org/10.1175/JCLI3838.1>, 2006.
- Zawada, D. J., Rieger, L. A., Bourassa, A. E., and Degenstein, D. A.: Tomographic retrievals of ozone with the OMPS Limb Profiler: algorithm description and preliminary results, *Atmos. Meas. Tech.*, 11, 2375–2393, <https://doi.org/10.5194/amt-11-2375-2018>, 2018.
- Zhu, Y., Toon, O. B., Jensen, E. J., Bardeen, C. G., Mills, M. J., Tolbert, M. A., Yu, P., and Woods, S.: Persisting volcanic ash particles impact stratospheric SO<sub>2</sub> lifetime and aerosol optical properties, *Nat. Commun.*, 11, 1–11, <https://doi.org/10.1038/s41467-020-18352-5>, 2020.